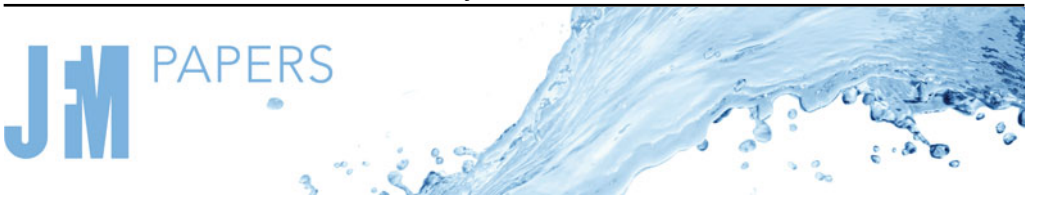
J. Fluid Mech. (2025), *vol.* 1018, A25, doi:10.1017/jfm.2025.10362



Vortical interactions in turbulent thermoacoustic systems

Ankit Sahay[1,2], **Muralikrishnan Gopalakrishnan Meena**[3] and **R.I. Sujith**[1,2]

[1]Department of Aerospace Engineering, Indian Institute of Technology Madras, Chennai 600 036, India

[2]Centre of Excellence for studying Critical Transitions in Complex Systems, Indian Institute of Technology Madras, Chennai 600 036, India

[3]National Center for Computational Sciences, Oak Ridge National Laboratory, Oak Ridge, TN 37831, USA

Corresponding author: Ankit Sahay, ankitsahay02@gmail.com

(Received 11 August 2024; revised 24 February 2025; accepted 3 June 2025)

This study examines the dynamics of vortical interactions and their implications for mitigating thermoacoustic instability in a turbulent combustor. The regions of intense vortical interactions are identified as vortical communities in the network space of weighted directed vortical networks constructed from two-dimensional experimental velocity data. One can expect vortical interactions in the combustor to be strongest near the moment of vortex shedding, as the shed vortices gradually weaken due to dissipation while convecting downstream. However, we show that, during the state of thermoacoustic instability, there is a non-trivial consistent phase lag of approximately 52° between the shedding of the coherent structures from the backward-facing step and the time instant when the vortical interactions attain their local maximum value. We explain this phase lag by investigating the correlation between acoustic pressure fluctuations, spatio-temporal dynamics of coherent structures and vortical interactions in the reaction field of the combustor. We also show the aperiodic variation of vortical interactions during the states of combustion noise and aperiodic epochs of intermittency. Furthermore, the spatio-temporal evolution of pairs of vortical communities with the maximum inter-community interactions provides insight into explaining the critical regions detected in the reaction field during the states of intermittency and thermoacoustic instability, also identified in previous studies. We further show that the most efficient suppression of thermoacoustic instability via air microjet injection is achieved when steady air jets are introduced to disrupt the maximum inter-community interactions present during the state of thermoacoustic instability.

https://doi.org/10.1017/jfm.2025.10362 Published online by Cambridge University Press

© UT-Battelle, LLC and the Author(s), 2025. Published by Cambridge University Press.

Key words: turbulent reacting flows, vortex interactions, vortex shedding

1. Introduction

The ubiquitous nature of turbulence around us warrants enduring efforts to understand the dynamics of turbulence. Turbulent flows contain definable flow configurations, known as coherent structures, that retain their identity over a considerable distance downstream (Hussain 1986). Among various research avenues, investigating large-scale coherent structures has garnered substantial attention for several decades (Fiedler 1988). As defined by Hussain (1983), coherent structures represent a connected, large-scale turbulent fluid mass with phase-correlated vorticity over its spatial extent. Consistent arguments have been made that coherent structures control the dominant aspects of transport (Zilitinkevich 1970), mixing (Yu & Schadow 1997), entrainment (Neamtu-Halic *et al.* 2019) and noise generation in turbulent shear flows (Mankbadi & Liu 1984).

Large-scale coherent structures play a pivotal role in various thermofluid systems, including combustion systems exhibiting thermoacoustic instability (Poinsot *et al.* 1987). Thermoacoustic instability is commonly observed in confined combustion chambers of engineering systems such as industrial burners, gas turbine combustors and rocket engines (Sujith & Pawar 2021). The emergence of large-scale coherent structures is one of the key mechanisms that drive thermoacoustic instability in combustion systems (Schadow & Gutmark 1992). In combustors prone to vortex-driven thermoacoustic instability, the roll-up of a coherent structure near the backward-facing step entrains a quantity of unburned fresh gases that burns rapidly in a very short period of time. This sudden combustion leads to an abrupt heat release that generates an acoustic wave, which produces an acoustic disturbance with a specific time lag (Candel, Durox & Schuller 2004). The acoustic perturbation causes the formation of the subsequent coherent structure in the shear layer formed close to the edge of the reactant inlet (Ho & Huerre 1984).

Most early research on the spatio-temporal dynamics in combustion systems exhibiting thermoacoustic instability centred on examining the periodic shedding of large-scale vortical structures (Coats 1996; Renard *et al.* 2000). Yu, Trouvé & Daily (1991) demonstrated that both the vortex and acoustic modes coexist in a backward-facing step configuration with a choked exit. Similar characteristics were also observed in the context of thermoacoustic instability in partially premixed flames within a one-sided backward-facing step combustor (Desai, Chakravarthy & Ramgopal 2010) and a bluff body combustor (Sivakumar & Chakravarthy 2008). Hong *et al.* (2013) demonstrated the emergence and growth of large-scale structures across various phases of acoustic pressure oscillations in a laboratory-scale backward-facing step combustor. Despite being one of the leading drivers of thermoacoustic instability in turbulent combustors, coherent structures remain a necessary evil in combustor design. They play a crucial role in flame holding and enhancing reactant mixing, leading to improved combustion efficiency. This underscores the ongoing need to deepen our understanding of the diverse roles played by coherent structures in turbulent combustors.

When studying the dynamics of coherent structures in the turbulent flow field of a combustor prone to thermoacoustic instability, these coherent structures rarely exist alone. Instead, various factors such as acoustic standing waves, flame stabilisation mechanisms and combustor boundaries often influence their behaviour. One of these crucial factors is the presence of multiple coherent structures in close vicinity in a turbulent flow field. These multiple coherent structures mutually interact with each other through

https://doi.org/10.1017/jfm.2025.10362 Published online by Cambridge University Press

vortical interactions. Following the shedding of vortices from the backward-facing step, the ensuing vortical interactions assume importance as the shed vortices propagate downstream. Investigating these vortical interactions is crucial for understanding the rich spatio-temporal dynamics of turbulent thermoacoustic systems, especially from the perspective of thermoacoustic instability control.

The presence of multiple coherent structures in the flow field of turbulent combustors, along with the corresponding presence of acoustic pressure and unsteady heat release rate fields, is a clear indicator of a complex system behaviour. A complex system is defined as a system with multiple interacting components whose behaviour cannot be inferred from the behaviour of its components (Smith, Brighton & Kirby 2003). The study of unsteady reactive fluid flows present in turbulent combustors often involves complex systems with high dimensionality. This high dimensionality necessitates advanced experimental and computational techniques to capture the intricate spatio-temporal dynamics and interplay of various physical processes. For such high-dimensional systems, complex networks offer a concrete mathematical framework for quantifying interactions between elements of a system (Barabási 2012).

In recent years, the adoption of complex networks has expanded to encompass the analysis and representation of fluid flows. The framework of complex networks has been harnessed to investigate induced velocity interactions among vortical elements (Nair & Taira 2015), Lagrangian motion of fluid elements (Ser-Giacomi *et al.* 2015; Hadjighasem *et al.* 2016), oscillator-based representation of the energy fluctuations (Nair, Brunton & Taira 2018), time series of fluid-flow properties (Zou *et al.* 2019), triadic interactions in turbulence (Gürcan 2017, 2018) and the effects of perturbations on time-varying vortical flows (Yeh, Gopalakrishnan Meena & Taira 2021). The application of complex network methodologies has expanded to investigate a wide array of turbulent flows, including two-dimensional isotropic turbulence (Taira, Nair & Brunton 2016), thermoacoustic oscillations in turbulent combustors (Krishnan *et al.* 2019*b*, 2021), wall turbulence (Iacobello, Scarsoglio & Ridolfi 2018), mixing in turbulent channel flow (Iacobello *et al.* 2019) and isotropic magnetohydrodynamic turbulence (Gürcan 2018). Iacobello, Ridolfi & Scarsoglio (2021) and Taira & Nair (2022) provide a comprehensive overview of the advancements in network-inspired analysis, modelling and control for a variety of unsteady fluid flows such as turbulent and vortical flows.

Since coherent structures are ubiquitous in fluid flows, applying clustering techniques for identifying and analysing vortical interactions in turbulent flows has gained significant traction in the last decade. Community detection methods have been successfully used in identifying vortical structures within turbulent flow fields (Murayama *et al.* 2018) and developing reduced-order models for laminar wake flows (Gopalakrishnan Meena, Nair & Taira 2018). In a separate study, Murayama *et al.* (2018) leveraged the spatial distribution of vortex strengths in the turbulence network and the community structure of the vorticity field to establish that the location of local minima in pressure fluctuations correspond to the proximity of the primary hub of the turbulence network to the injector rim of the combustor. Later, Kawano *et al.* (2023) extended the concept of clustering of complex networks in thermofluid systems to analyse the spatio-temporal dynamics of a model single-element rocket combustor using a spatial network constructed from flux balance of acoustic energy. The authors demonstrated that the development of spatially large communities exhibiting strong connections plays a crucial role in driving thermoacoustic instability. The cumulative body of research conducted thus far has progressively deepened our comprehension of the intricate spatio-temporal dynamics of thermoacoustic systems.

https://doi.org/10.1017/jfm.2025.10362 Published online by Cambridge University Press

Previous studies have predominantly concentrated on the shedding dynamics of coherent structures and their interactions with unsteady flame behaviour. However, there is little discussion on the dynamics of vortical interactions in turbulent thermoacoustic systems. The interaction among vortical structures has been investigated only for non-reacting flows (Nair & Taira 2015). A natural initial hypothesis for reacting flows in turbulent combustors might be that vortical interactions are strongest when the vortical structures first detach from the backward-facing step. This is because the magnitude of vorticity corresponding to the detached coherent structure is at its maximum at the instant of its shedding. As these coherent structures convect downstream with the flow, their strength decreases due to the dissipation of vorticity into the surrounding flow field.

However, we show that the vortical interactions attain their maximum values at a significant distance downstream from the backward-facing step during the state of thermoacoustic instability. From the context of phase calculated for acoustic pressure oscillations during the state of thermoacoustic instability, there is a phase lag of approximately 52° between the shedding of coherent structure from the backward-facing step and the instance when the vortical interactions attain their maximum value. To comprehensively investigate the dynamics of vortical interactions in the turbulent combustor, we employ community detection and community-based network reduction techniques on time-varying vortical networks to establish the interplay between such vortical interactions and the global acoustic dynamics exhibited by the turbulent combustor. Finally, we discuss the role of vortical interactions in the occurrence of critical regions that are suitable for open-loop control via air microjet injection. We close our discussions by demonstrating that the state of maximum suppression of thermoacoustic instability through open-loop control corresponds to the disruption of regions of vortical communities with the strongest inter-community interactions.

2. Experimental set-up

Experiments were conducted in a bluff body stabilised combustor with a rectangular cross-section, possessing dimensions of $1100 \times 90 \times 90$ mm^3. The combustor comprises a settling chamber, a burner section and a rectangular duct (figure 1*a*). In order to protect the flow entering the combustor from upstream disturbances, compressed air first enters the settling chamber. The fuel (liquefied petroleum gas – 60 % butane + 40 % propane) is injected upstream of the backward-facing step (59 mm upstream of the bluff body) through four 1 mm diameter holes bored symmetrically around the circular shaft holding the bluff body in the combustor. Thus, the fuel gets partially mixed in the air stream as it enters the combustor. We use an 11 kV ignition transformer to spark ignite the partially premixed air–fuel mixture at the backward-facing step. The flame stabilisation device is a bluff body in the shape of a circular disc with a diameter of 47 mm and a thickness of 10 mm and is positioned 35 mm downstream of the backward-facing step. The combustion products are exhausted through a long duct into the atmosphere via a decoupler. The decoupler is a large chamber used to keep the combustor exit at an acoustically open boundary state ($p' \approx 0$) and decouple the combustor from external perturbations.

Digital mass flow controllers (Alicat Scientific – MCR Series, 100 SLPM model for fuel flow, 4000 SLPM for the main air flow) are used to control the flow rates of air and fuel. The mass flow controllers have an uncertainty of ± (0.8 % of reading + 0.2 % of full scale). In the experiments, the fuel flow rate $\dot{m}_f$ is maintained at a constant value ($\dot{m}_f = 30 \pm 0.44$ standard litre per minute (SLPM)), and the air flow rate $\dot{m}_a$ is varied ($480 \pm 7.84 \leqslant \dot{m}_a \leqslant 780 \pm 10.24$ SLPM) to change the global equivalence ratio ($\phi = (\dot{m}_f/\dot{m}_a)_{actual}/(\dot{m}_f/\dot{m}_a)_{stoichiometric}$), of the reactant mixture. The global

https://doi.org/10.1017/jfm.2025.10362 Published online by Cambridge University Press

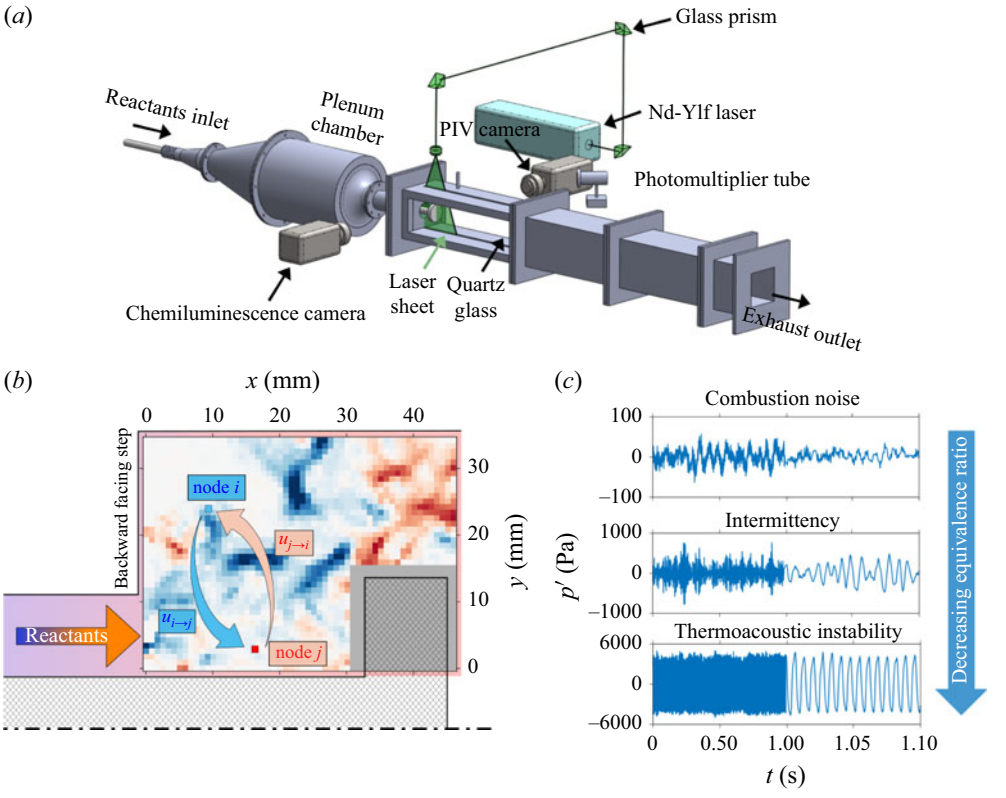


Figure 1. (*a*) Schematic diagram of the experimental set-up. We simultaneously acquire the acoustic pressure measurement and high-speed two-component particle image velocimetry (2C PIV) data for the current study. (*b*) Interactions between two vortical elements in the vorticity field were calculated from the velocity field in the turbulent combustor obtained experimentally using 2C PIV. Here, $u_{i\to j}$ denotes the velocity induced by the node i on node j, and *vice versa*. The cross-hatched region indicates the bluff body and the shaft holding the bluff body. (*c*) Time series of acoustic pressure fluctuations during the states of combustion noise, intermittency and thermoacoustic instability.

equivalence ratio ϕ is the control parameter in the current study and is varied from 0.97 to 0.57. The maximum uncertainty in the calculation of ϕ is ± 0.02. The Reynolds number (calculation based on the flow conditions of the air at the inlet of the combustor) varies in the range $19\,300 \leqslant Re \leqslant 31\,300$, with a maximum uncertainty of ± 400 (1.28 %). We measure the acoustic pressure fluctuations $p'(t)$ using a PCB103B02 piezoelectric transducer (sensitivity: 217.5 mVkPa^{-1} and uncertainty: ± 0.15 Pa) mounted on the combustor wall 20 mm downstream of the backward-facing step.

We perform high-speed two-component particle image velocimetry (2C PIV) to acquire the two components of velocity (v_x: streamwise parallel to the flow direction and v_y: perpendicular (cross-stream) to the flow direction). The reactive flow field is seeded with $\approx$1 mm sized TiO_2 particles (Kronos make product – 1071). The Stokes number ($Stk = (t_0 u_0)/l_0$) of the seeded flow, where t_0 is the characteristic response time of the particle, u_0 is the gas velocity and l_0 is the characteristic dimension of the particle, is 7×10^{-4}. For such low values of Stk ($Stk \ll 1$), the seeded particles faithfully follow the streamlines (Raffel *et al.* 1998). We use a single cavity double pulsed Nd:YLF laser (with 527 nm and a pulse width of 250 ns) to illuminate the flow through a narrow quartz window ($400 \times 20 \times 10$ mm^3) on the top wall of the combustion chamber.

https://doi.org/10.1017/jfm.2025.10362 Published online by Cambridge University Press

To capture the Mie scattering light from the seeding particles, we use a high-speed CMOS camera (Photron FASTCAM SA4) synchronised with the laser pulses. A short band pass optical filter (centred at 527 nm with 12 nm Full Width at Half Maximum) is mounted in front of the lens to capture the Mie scattered light. We record 3797 Mie Scattering image pairs for approximately 2 s. The physical region of interest used for the analysis of 2C PIV is located just downstream of the backward-facing step and slightly above the bluff body shaft, as shown in figure 1(*b*). The Mie scattering images are processed using PIVview2C software (PIVTEC GmbH). We use the cross-correlation algorithm to calculate the velocity fields (Raffel *et al.* 1998).

In the bluff body stabilised turbulent combustor considered in the present study, the dynamics exhibited by the combustor transitions from the state of combustion noise to the state of thermoacoustic instability via the state of intermittency as the global equivalence ratio of the reactant mixture is decreased from $\phi = 1$ in a quasi-static manner. Figure 1(*c*) shows the time trace of acoustic pressure fluctuations during the three dynamical states of combustor operation, where the equivalence ratio varies from near stoichiometry to conditions corresponding to the state of thermoacoustic instability. When the equivalence ratio is close to stoichiometry, the temporal dynamics of the combustor is characterised by low-amplitude, aperiodic pressure fluctuations. This condition of combustor operation is referred to as combustion noise. The turbulent combustor exhibits the state of intermittency as the equivalence ratio is decreased. During the state of intermittency, the time series of acoustic pressure consists of epochs of high-amplitude periodic oscillations appearing in a seemingly random manner between epochs of low-amplitude aperiodic fluctuations (Nair, Thampi & Sujith 2014). The onset of thermoacoustic instability, characterised by periodic acoustic pressure oscillations of high amplitude, occurs as the equivalence ratio is decreased further.

Once the raw velocity data acquired during the three different dynamical states mentioned above are processed, the final velocity data corresponding to the region of interest at each time instant have the following dimensions during different states of the combustor operation:

(i) Combustion noise –37.35 mm × 49.8 mm, corresponding to 45 × 60 pixels.
(ii) Intermittency –34.23 mm × 46.45 mm, corresponding to 42 × 57 pixels.
(iii) Thermoacoustic instability –34.86 mm × 46.48 mm, corresponding to 42 × 56 pixels.

The different dimensions of the regions of investigation (ROIs) are attributed to experimental constraints. The primary differences between the different regions occur on the top and right sides of the flow field. The differences in ROIs during the three dynamical states do not significantly affect the results presented in the present work. The crucial vortical structures, which are central to understanding the vortical interactions during the different dynamical states exhibited by the combustor, are consistently captured within the ROIs. An in-depth elucidation of the preprocessing and post-processing algorithms employed for the analysis of 2C PIV data, as well as a comprehensive discussion concerning velocity uncertainties, can be found in George *et al.* (2018). Additional details are available in the supplementary material provided by Krishnan *et al.* (2019*a*).

Despite the inherently three-dimensional nature of the combustor flow field in this study, we expect a reasonably axisymmetric flow during the state of thermoacoustic instability due to the longitudinal instability mode and the circular boundary of the backward-facing step. Additionally, the periodic shedding of coherent structures from the backward-facing step, a key flow dynamic relevant to this study, is accurately captured by

https://doi.org/10.1017/jfm.2025.10362 Published online by Cambridge University Press

the 2C PIV measurements. Even during states of combustion noise and intermittency, we expect the velocity data obtained from the 2C PIV measurements to qualitatively represent the velocity values in the three-dimensional flow field. The turbulent combustor is indeed a high-dimensional system with millions of degrees of freedom. The low-dimensional vorticity field calculated via 2C PIV measurements constitutes one of the many system variables that can be utilised to infer the spatio-temporal dynamics of the high-dimensional turbulent system.

3. Complex network description of vortical interactions and community detection

Taira *et al.* (2016) introduced a weighted complex network analysis to characterise the vorticity interactions in a two-dimensional decaying isotropic turbulent flow field obtained from direct numerical simulations. The nodes of the network are the cells in the computational grid representing the vortical elements in the flow field, and the weight of the link is the velocity induced by the vortical elements (figure 1*b*). The induced velocities are calculated using the Biot–Savart law (Tietjens & Prandtl 1957; Malmendier & Reid 2020)

$$u_{i\to j} = \frac{|\omega_i|\Delta S}{2\pi|\boldsymbol{r}_j - \boldsymbol{r}_i|}, \quad i \neq j, \tag{3.1}$$

where $u_{i\to j}$ denotes the magnitude of the velocity induced by vortical node i on a vortical node j, ω_i denotes the vorticity value of the vortical element assumed to be present at node i, ΔS denotes the area of a single computational cell which is assumed to have a vortical element and $|\boldsymbol{r}_j - \boldsymbol{r}_i|$ indicates the distance between nodes j and i. The weighted adjacency matrix $A \in \mathbb{R}^{n\times n}$ for this vortical flow network is defined as

$$A_{ij} = \begin{cases} w_{ij}, & i \neq j \\ 0, & i = j, \end{cases} \tag{3.2}$$

where w_{ij} is the edge weight given by

$$w_{ij} = \alpha u_{i\to j} + (1-\alpha)u_{j\to i}, \tag{3.3}$$

with $\alpha \in [0, 1]$ being a parameter to capture the induced velocity direction to construct the vortical network. A value $\alpha = 0$ or 1 gives a directed adjacency matrix, whereas $\alpha = 1/2$ yields a symmetric adjacency matrix corresponding to an undirected network. The statistics of the final results presented in this study show minimal variation with changes in α, as detailed in Appendix D. In this study, we use $\alpha = 0$ to preserve the notion of directionality of induced velocity. Adding directions to the edges helps to differentiate between the influential and influenced vortical nodes. Thus, in the present study, we define the weighted directed vortical network as

$$A_{ij} = u_{j\to i}. \tag{3.4}$$

The above formulation in (3.4) gives an asymmetric adjacency matrix with non-binary entries, representing a weighted directed network. The velocity uncertainty of 1.25 % to 2.5 % due to 2C PIV data analysis translates to an uncertainty of 0.0139 to 0.0167 ms^{-1} in the edge weights of the adjacency matrix (considering a velocity of 5 ms^{-1} of the fluid particles during the state of thermoacoustic instability). The adjacency matrix contains zero values on its diagonal due to the absence of velocity influence between vortical nodes onto themselves. As every vortical node is interconnected with all others, the vortical network is a complete graph.

https://doi.org/10.1017/jfm.2025.10362 Published online by Cambridge University Press

It is not easy to characterise the interactions between the vortical components since the spatio-temporal dynamics exhibited by the turbulent combustor is high-dimensional in nature. Analysis, simulation and modelling of the dynamics on such large networks demand massive amounts of processing power and necessitate decreasing the computational complexity of the problem while preserving the fundamental physics. To reduce the high dimensionality of the vortical interactions, we detect communities on the time-varying vortical networks constructed for the three dynamical states. Communities are modular clusters of nodes that are densely connected. Communities are derived from decomposing the network into sub-components that are internally strongly connected but externally only weakly connected (Newman & Girvan 2004).

Modularity maximisation is a technique for community detection that is frequently used to identify communities (Newman & Girvan 2004). This technique seeks to optimise the modularity quality function, M, by dividing a network's nodes into K non-overlapping communities, $C_1, C_2, \ldots, C_K$. Modularity, M, measures the proportion of edges in a network that link nodes within the same community in excess of the expected proportion of such edges if the network had the same community structure but random connections between the nodes. To receive a higher M score, the communities that a partition defines should be internally more dense than what can be predicted by chance. The community structure of a network is, therefore, assumed to be best represented by the division that gets the highest value of M. Modularity M is given by

$$M = \frac{1}{2n_e} \sum_{ij} \left[A_{ij} - \gamma_M \frac{s_i^{in} s_j^{out}}{2n_e} \right] \delta(c_i, c_j), \tag{3.5}$$

where

$$s_i^{out} = \sum_j A_{ji} \quad \text{and} \quad s_i^{in} = \sum_j A_{ij}. \tag{3.6a,b}$$

Here, s_i^{out} and s_i^{in} denote the out- and in-strengths of a node, respectively. In (3.5), γ_M is the resolution parameter to detect the presence of large or small communities in the network (Reichardt & Bornholdt 2006; Fortunato & Barthelemy 2007), n_e is the total number of edges in the network, $\delta(c_i, c_j)$ is the Kronecker delta, $c_i \in \hat{C}_k$ is the label of the community to which node i is assigned and $\hat{C}_k$ is the set of k community in the network. Here, $k = 1, 2, \ldots, K$, with K being the total number of communities; K is not a user-defined variable, and is determined by the community detection algorithm used. Various algorithms are available to detect the communities in a network (Fortunato 2010).

In the present study, we use the modularity maximisation method introduced by Blondel *et al.* (2008) to detect communities. We refer to these detected communities on vortical networks as vortical communities (Gopalakrishnan Meena *et al.* 2018). The fluid elements with high vorticity play an important role in the dynamics exhibited by the turbulent combustor. Thus, we neglect the effects of fluid elements with low vorticity. We consider only those spatial locations for nodes in vortical communities that exhibit vorticity magnitudes greater than $|\omega| = 456$, 380 and 843 s^{-1} during the states of combustion noise, intermittency and thermoacoustic instability, respectively. Further details on calculations for these threshold values are provided in Appendix A.

We use a sample network as shown in figure 2 to demonstrate the dimensionality reduction method we use in the current study. In figure 2, we consider a sample random modular graph constructed using methods discussed in Lancichinetti, Fortunato & Radicchi (2008). Each node i has a scalar weight, γ_i, associated with it. This scalar weight

https://doi.org/10.1017/jfm.2025.10362 Published online by Cambridge University Press

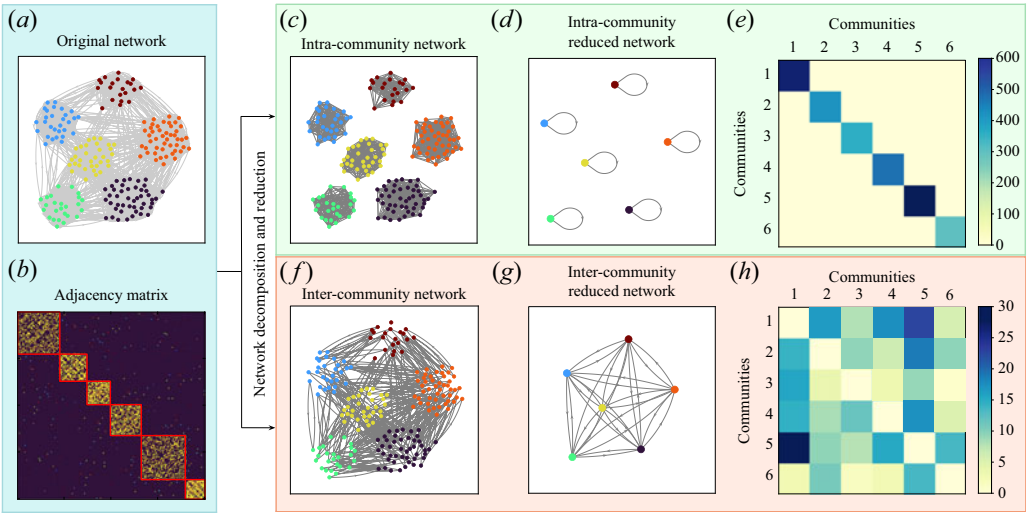


Figure 2. An overview of community-based reduction of a representative directed complex network. (*a*) A random modular graph with six communities is constructed according to the Fruchterman–Reingold algorithm (Fruchterman & Reingold 1991), and the corresponding adjacency matrix is shown in (*b*). The modular nature of the network manifests as a block structure in the adjacency matrix. The original network can be decomposed into two sub-networks: (*c*) an inter-community network comprising edges present only across different communities, and (*f*) an intra-community network comprising edges present only within the individual communities. (*d*,*g*) Each community can be considered as a single node. All the edges between a pair of communities and within each community can be summed up to obtain (*d*,*e*) a reduced inter-community network and (*f, g*) a reduced intra-community network. The adjacency matrix of the reduced inter-community network is shown in (*h*).

is analogous to the vorticity value of each fluid element in a flow system. In figure 2(*b*), we cluster the nodes into network communities using the Louvain algorithm (Blondel *et al.* 2008). The details of implementing the Louvain algorithm are given in Appendix B. We decompose the original network into inter-community and intra-community networks in figures 2(*c*) and 2(*f*), respectively. The inter-community network is further condensed to weighted-centroid-based network (Gopalakrishnan Meena *et al.* 2018) in figure 2(*d*). The weighted centroids of each community are calculated using

$$\boldsymbol{\xi}_k = \frac{\sum\limits_{i \in C_k} \gamma_i \boldsymbol{r}_i}{\sum\limits_{i \in C_k} \gamma_i}, \quad k = 1, 2, \ldots, m, \tag{3.7}$$

and the sum of all the scalar weights belonging to nodes of each community

$$\Gamma_k = \sum_{i \in C_k} \gamma_i, \tag{3.8}$$

is concentrated at the community centroid, reducing the community to a single node at the respective community centroid. Here, $\boldsymbol{r}_i$ denotes the position vector of each node i and Γ_k is the node attribute of each node in the community-based reduced network, where k refers to the k^{th} community present in the original network. By employing this framework for the vortical network, we use the weight and position vector of each community centroid to reconfigure the vortical network and reduce the dimensions of the system. It is important to note that the sample network depicted in figure 2 is a directed network, as evident from the asymmetry of its reduced adjacency matrix shown in figure 2(*e*). This figure is included

https://doi.org/10.1017/jfm.2025.10362 Published online by Cambridge University Press

solely to illustrate the concepts of inter-community and intra-community links and does not represent any of the directed networks analysed in the present manuscript.

4. Results and discussion

We initially examine the phase-averaged vortical interactions during the state of thermoacoustic instability. The periodic nature of a self-organised flow field during this dynamical state facilitates a clear interpretation of results. The phase-averaged results obtained from the state of thermoacoustic instability also help us proceed further with the investigation of time-varying vortical networks for all the dynamical states exhibited by the combustor.

4.1. *Phase-averaged analysis of strongest influential communities*

A significant implication of the shedding of coherent structures in unsteady fluid flows is the presence of a periodic fluctuating dynamics. The resulting periodic forces can inflict destructive, unsteady loading on the structure of the physical systems and may lead to catastrophic incidents. Since coherent structures are related to the regions of high vorticity in the hydrodynamic field, an essential step in understanding the role of interaction among regions of high vorticity toward such periodic dynamics is to use complex networks to analyse the outward influence of vortical communities on other fluid elements. To this end, we use phase-averaged analysis during the state of thermoacoustic instability to understand the variation in the location and strength of the communities with maximum outward influence, as shown in figure 3.

We use the participation coefficient P to quantify the outward influence of nodes present in vortical communities (Guimerà & Amaral 2005). The participation coefficient is a relative measure of the inter-community strength of a node and provides an indication of how well distributed the edges of a node are amongst all communities other than its own. The participation coefficient P_i of node i is given by

$$P_i = 1 - \sum_k \left(\frac{s_i^k}{s_i} \right)^2 , \tag{4.1}$$

where s_i is the total strength of node i, and s_i^k is the strength of node i to influence all nodes in community k; s_i^k and P_i can be evaluated for both in- and out-edges. Since we are interested in understanding the influence of a vortical community on other fluid elements, we evaluate the out-edge-based measures in the current study to understand the outward influencing properties of the fluid elements.

We plot the locations of weighted centroids of communities with maximum outward participation coefficient at each phase in figure 3(*b*). Figure 3(*c*) shows the phase-averaged distribution of P_i of all the nodes belonging to the community with the maximum outward inter-community interaction. We use phase-averaged P_i instead of calculating P_i from phase-averaged vorticity fields to ensure that community affiliations that are critical for meaningful P_i values are preserved and utilised to calculate P_i before phase averaging is done. Using phase-averaged vorticity fields to calculate P_i would smooth out essential inter-community interactions and lead to loss of information on community affiliations. Around 50 realisations for each phase of the cycle were averaged, resulting in an ensemble-averaged quantity of interest at each of the 8 phases ($\phi = 0°$ to 315° in intervals of 45°). The phase angle $\phi = 0°$ corresponds to the local minima of acoustic pressure fluctuations, p', and is shown in figure 3(*a*). We also plot the phase-averaged distribution of vorticity $\overline{\omega}_\phi$

https://doi.org/10.1017/jfm.2025.10362 Published online by Cambridge University Press

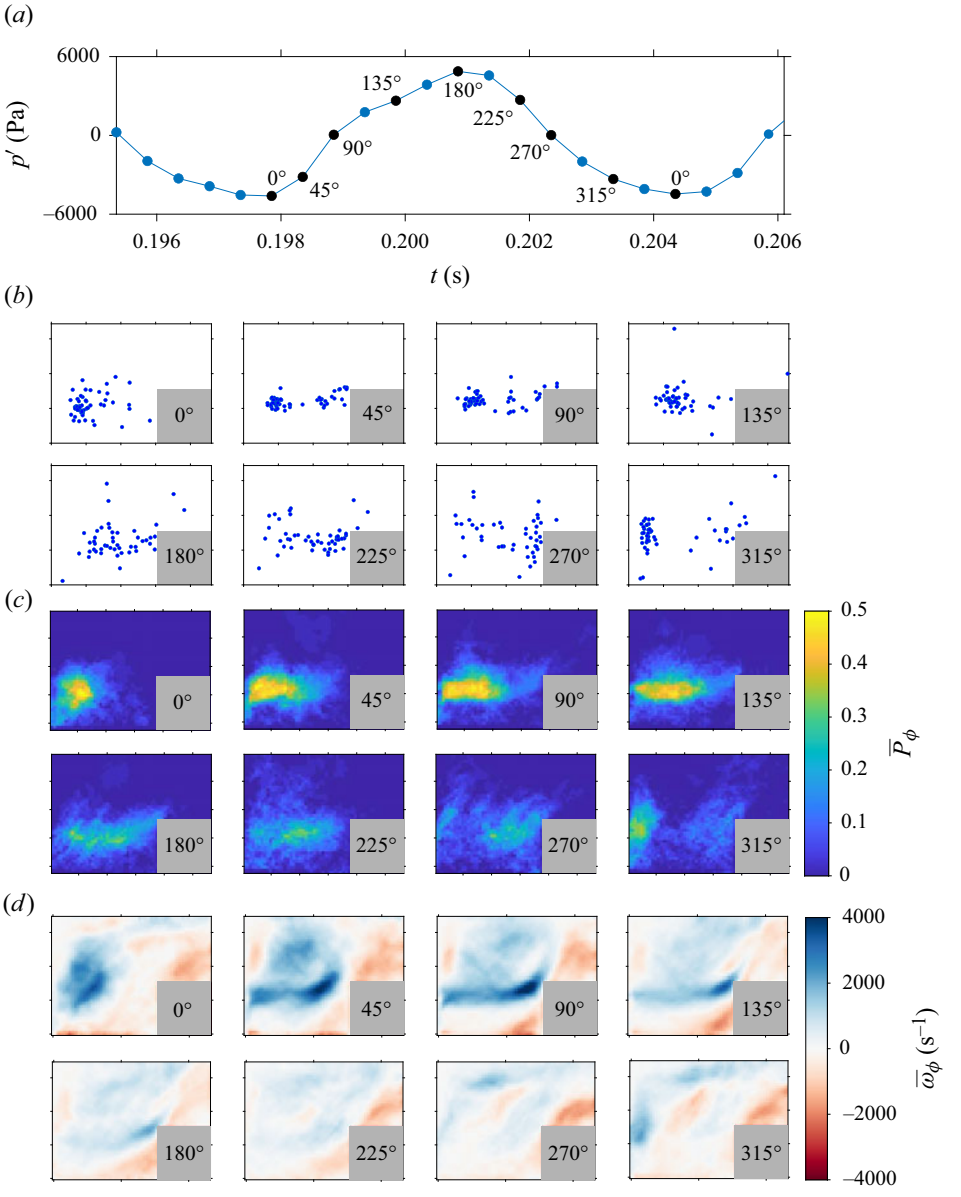


Figure 3. (*a*) Time instances denoting the phases in one acoustic cycle during the state of thermoacoustic instability. (*b*) Shows the locations of weighted centroids of communities with maximum outward participation coefficient at each phase. (*c*) Phase-averaged fields of participation coefficients P corresponding to the nodes in communities having the maximum P values at the indicated phases of the acoustic cycle during the state of thermoacoustic instability. The participation coefficient quantifies the influence of a single node on communities other than its own. We also plot the phase-averaged distribution of vorticity in (*d*). The mismatch between the locations of high phase-averaged participation coefficient ($\overline{P}_\phi$) and high phase-averaged vorticity ($\overline{\omega}_\phi$) for phases 45° to 135° points to the inherent difference between the roles of vortical interactions and vorticity. Here, $\overline{P}_\phi$ reflects the combined influence of the strength and position of the vortical elements in the network space. However, $\overline{\omega}_\phi$ is an attribute of the individual vortical elements and does not depend on the other vortical elements.

https://doi.org/10.1017/jfm.2025.10362 Published online by Cambridge University Press

in figure 3(*d*) to interpret the phase-averaged distribution of the participation coefficient $\overline{P}_\phi$ from the perspective of hydrodynamics present in the flow field during the state of thermoacoustic instability.

We observe a region of high phase-averaged participation coefficient $\overline{P}_\phi$ near the backward-facing step at $\phi = 0°$. This region of high $\overline{P}_\phi$ is due to the coherent structure shedding from the backward-facing step at the same phase angle. However, this coherent structure continues to convect downstream whereas the region of high $\overline{P}_\phi$ continues to remain near the backward-facing step at the subsequent phase angles of 45° to 180°. This observation is perplexing, as one would intuitively anticipate that regions characterised by high vorticity would coincide with the regions exhibiting high participation coefficients. This hypothesis arises from the understanding that regions exhibiting larger vorticity values will have larger vortical influence over other regions in the flow field.

We attribute this difference to the interpretation of participation coefficient P_i from the network and vorticity ω from the point of view of the hydrodynamics. The strength of the participation coefficient P_i depends on multiple factors: (i) the vorticity of the node, (ii) the size of the community to which the node belongs and (iii) the spatial distance between the node and other communities. However, ω is an attribute of the node i and does not depend on the other vortical elements. Thus, although the regions of high vorticity continue to move downstream as the phase angle increases from 0° to 135°, the regions of highest $\overline{P}_\phi$ values do not spatially match with the regions of highest $\overline{\omega}_\phi$ values. This spatial mismatch occurs because the nodes exhibiting the strongest $\overline{P}_\phi$ values remain in the middle of the spatial domain (seen in figures 3*b* and 3*c*), as this middle region minimises the distance to other communities, thereby enhancing the outward inter-community influence of the communities present in this region. This spatial mismatch between regions of highest $\overline{\omega}_\phi$ and highest $\overline{P}_\phi$ between the phases 45° to 135° indicates that, in addition to tracking the downstream convection of the coherent structure shed from the backward-facing step, spatial proximity of other regions of high vorticity must also be taken into account to understand the spatio-temporal behaviour of vortical interactions present during the state of thermoacoustic instability.

At further phase angles of 180° to 270°, the values of participation coefficients decrease significantly, corresponding to the decrease in the vorticity values present in the flow domain. Finally, at the phase angle value of 315°, we observe the emergence of a region of high $\overline{P}_\phi$ values near the backward-facing step, along with an increase in the values of vorticity $\overline{\omega}_\phi$ in the same region. This occurs just before the coherent structures are again shed at the acoustic pressure minima ($\phi = 0°$) of the next periodic cycle. The spatio-temporal dynamics of $\overline{P}_\phi$ and ω is subsequently repeated in all acoustic cycles during the state of thermoacoustic instability.

Values of $\overline{P}_\phi$ can be interpreted as an indicator of the combined influence of strength and position of the vortical elements present in the spatial field under consideration. It is possible that a fluid element with a significantly high vorticity magnitude located at the periphery of the spatial domain can exert comparatively less influence on other fluid elements than a fluid element with a lower vorticity magnitude but located towards the centre of the spatial domain. Although this information is embedded in the formulation of Biot–Savart law, and thus, in the edge weights of the adjacency matrix, $\overline{P}_\phi$ brings out the combined influence of the strength and position of the vortical elements attributed to various communities more clearly. As we move ahead, we examine the spatio-temporal dynamics of vortical communities to understand the reason behind the discrepancy between regions of vorticity and regions of maximum participation coefficient.

https://doi.org/10.1017/jfm.2025.10362 Published online by Cambridge University Press

4.2. *Spatio-temporal evolution of maximum-interacting pairs of vortical communities*

In this section, we analyse the connection between the acoustic pressure oscillations, the network measures representing the spatio-temporal evolution of the maximum-interacting pair of vortical communities and the corresponding vorticity distribution present in the reactive flow field. It is crucial to study the vorticity distribution as the vortex shedding within a turbulent combustor is closely related to the acoustic pressure fluctuations observed within the combustion chamber.

The spatio-temporal dynamics of vortical interactions is captured using tools from complex network theory discussed in § 3. We quantify the spatio-temporal evolution of the maximum-interacting pair of vortical communities using the average and maximum of all inter-community interactions present at any given instant of time, denoted by $A_{r,mean}$ and $A_{r,max}$, respectively. The subscript r indicates that the quantities $A_{r,mean}$ and $A_{r,max}$ have been calculated from the reduced adjacency matrix. We compare the temporal evolution of p' fluctuations with the average and maximum of all the inter-community interactions during all the dynamical states exhibited by the turbulent combustor. Since the acoustic pressure remains approximately constant throughout the reaction field of the combustor (George *et al.* 2018), tracking the temporal evolution of the average of all inter-community interactions allows us to correlate the dynamics of the entire reaction field with the acoustic pressure fluctuations. On the other hand, tracking the maximum of all the inter-community interactions will help us understand the spatio-temporal evolution of the most influential pair of vortical communities. Subsequently, this spatio-temporal evolution of vortical communities is correlated with different phases of an acoustic pressure cycle.

4.2.1. *Combustion noise*

In figure 4, we compare the temporal evolution of p' fluctuations with the average and maximum of all the inter-community interactions during the state of combustion noise. The time series of acoustic pressure oscillations and the network measures are shown in figure 4(*a*). The zoomed-in versions are shown in figure 4(*b*,*c*). We observe that the time series of network measures is aperiodic during the state of combustion noise. The aperiodic nature of the inter-community interactions results from the incoherent spatio-temporal distribution of the vortical communities present during the state of combustion noise.

In figure 4(*d*), we show the spatio-temporal evolution of the vorticity distribution and vortical communities with the maximum inter-community interactions across three representative instants during the state of combustion noise. At each time instant, the pair of vortical communities consists of two different communities with two inter-community edges directed from, say, community 1 to community 2, and *vice versa*. Community 1 exhibits outward inter-community strength distribution towards community 2 with $k_{out,1}$ values, whereas community 2 exhibits outward inter-community strength distribution towards community 1 with $k_{out,2}$ values. Thus, in figure 4(*d*), the direction of the maximum inter-community interaction is from the community marked with $k_{out,1}$ values to the community marked with $k_{out,2}$ values.

The ranges of $k_{out,1}$ and $k_{out,2}$ are indicated in the colour bars. The spatial distribution of the pair of communities in figure 4(*d*) indicates that most of the vortical communities with maximum inter-community interactions are located above the bluff body. This is due to a large concentration of coherent structures shed from the upstream tip of the bluff body during the state of combustion noise. Furthermore, the vortical communities

https://doi.org/10.1017/jfm.2025.10362 Published online by Cambridge University Press

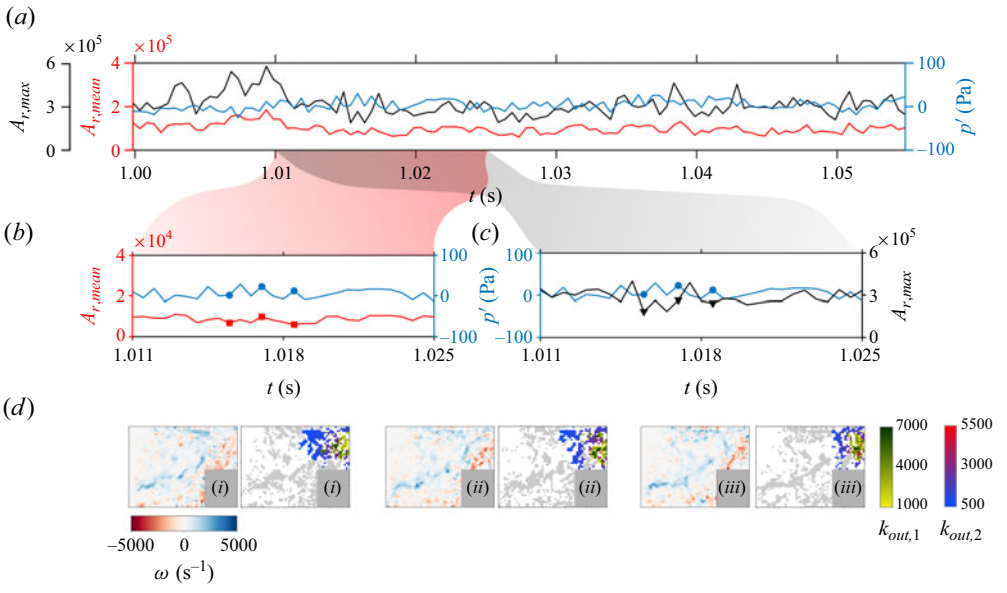


Figure 4. (*a*) Time series showing the variation of p' fluctuations and network measures (mean $A_{r,mean}$, and maximum $A_{r,max}$ of all inter-community interactions) during the state of combustion noise. The acoustic pressure fluctuations are marked in blue. The zoomed-in versions are shown in (*b–c*). The two shaded regions indicate the portion in (*a*) used for the time series shown in (*b–c*). The vorticity field and the corresponding spatial distribution of the inter-community in- and out-strengths between the pair of communities with the maximum inter-community interaction at each of the representative time instants marked in (*b–c*) are shown in (*d*). The grey regions represent other vortical communities that have lower inter-community interactions. The colour bars represent the out-strengths of the pair of communities with maximum inter-community interactions, denoted by $k_{out,1}$ and $k_{out,2}$, respectively. The direction of the maximum inter-community interaction is from the community marked with $k_{out,1}$ values to the community marked with $k_{out,2}$ values. The aperiodic nature of the network measures reflects the aperiodic nature of hydrodynamic interactions present in the reaction field. Due to the shedding of significant vortices from the upstream tip of the bluff body, the pair of communities with the maximum inter-community interaction are always present above the bluff body.

shown are quite fragmented in space due to small regions of high vorticity present in the spatial domain. This contrasts the large spatially coherent vortical communities present during the aperiodic epochs of intermittency, as discussed in the next subsection. The spatial fragmentation of communities present in different dynamical states is discussed and compared in Appendix C.

4.2.2. *Aperiodic epoch of intermittency*

Similar to the aperiodic dynamics of inter-community interactions observed during the state of combustion noise, we observe aperiodicity during the aperiodic epoch of intermittency in figure 5. Figure 5(*b*,*c*) show the zoomed-in versions of the time series of acoustic pressure fluctuations and network measures shown in figure 5(*a*). Figure 5(*d*) shows the vorticity field and the corresponding pair of maximum-interacting communities in the spatial domain. The aperiodic nature of the network measures shown in figure 5(*b*,*c*) reflects the aperiodicity in the spatio-temporal evolution of vortical interactions present during the aperiodic epoch of intermittency. In figure 5(*d*), we observe large regions of low vorticity present in the reaction field, unlike the small localised regions of high vorticity present during the state of combustion noise. Thus, compared with the fragmented nature

https://doi.org/10.1017/jfm.2025.10362 Published online by Cambridge University Press

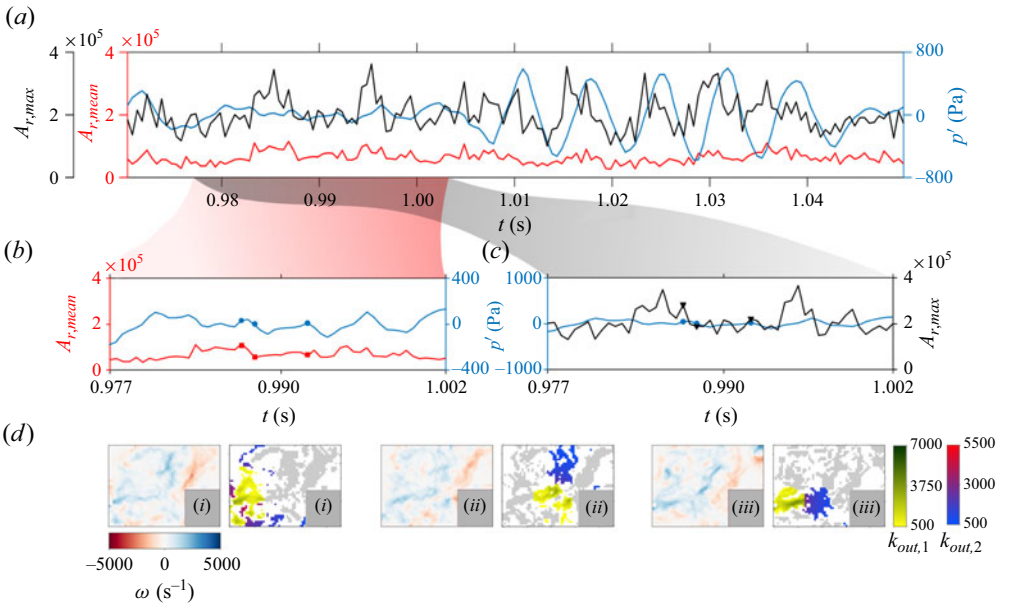


Figure 5. (*a*) Time series showing the variation of p' fluctuations and network measures (mean $A_{r,mean}$, and maximum $A_{r,max}$ of all inter-community interactions) during an aperiodic epoch of intermittency. The zoomed-in versions are shown in (*b–c*). The two shaded regions indicate the portion in (*a*) used for the time series shown in (*b–c*). The vorticity field and the corresponding spatial distribution of the inter-community in- and out-strengths between the pair of communities with the maximum inter-community interaction at each of the representative time instants marked in (*b–c*) are shown in (*d*). The aperiodic nature of vortical interactions present in the reaction field causes the network measures to be aperiodic. Correspondingly, there is no specific trend in the position of the pair of communities with maximum inter-community interaction, as seen in (*d*).

of vortical communities present during the state of combustion noise, we observe large spatially coherent vortical communities during the aperiodic epoch of intermittency.

Furthermore, the average of the inter-community node strengths is slightly lower than that observed during combustion noise (refer to the variation of $A_{r,mean}$ in figure 4*a*). The lower values of $A_{r,mean}$ observed during the aperiodic epoch of intermittency are due to the large spatial extent of low vorticity regions present during the aperiodic epoch of intermittency, in contrast with the small spatial extent of high vorticity regions present during combustion noise. The difference in the values of $A_{r,mean}$ observed during the states of combustion noise and the aperiodic epoch of intermittency is an artefact of different spatio-temporal reaction fields present during the two dynamical states, even though the acoustic pressure fluctuations are of a similar order of magnitude during these two dynamical states.

4.2.3. *Periodic epoch of intermittency*

During the periodic epoch of intermittency, we observe that spatially coherent regions with large vorticity magnitude begin to emerge in the reaction field (figure 6). Figures 6(*a*) and 6(*b*,*c*) show the time series of acoustic pressure fluctuations and network measures and their zoomed-in versions during a periodic epoch of intermittency, respectively. Figure 6(*d*) shows the vorticity field and the corresponding pair of maximum-interacting communities in the spatial domain. We notice that the mean of inter-community interactions $A_{r,mean}$ shows an aperiodic behaviour during the periodic epoch on intermittency. Taking the mean of all inter-community interactions possibly smears the

https://doi.org/10.1017/jfm.2025.10362 Published online by Cambridge University Press

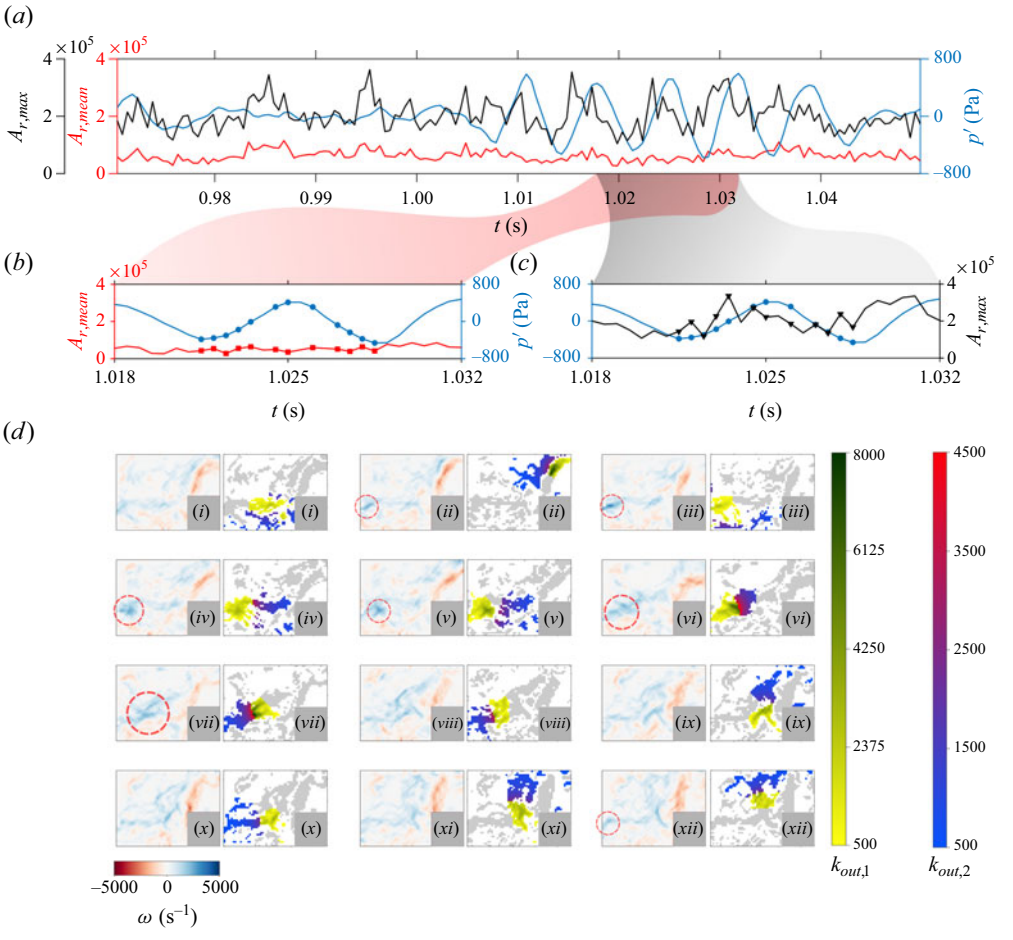


Figure 6. (*a*) Time series showing the variation of p' fluctuations and network measures (mean $A_{r,mean}$, and maximum $A_{r,max}$ of all inter-community interactions) during a periodic epoch of intermittency. The acoustic pressure fluctuations are marked in blue. The zoomed-in versions are shown in (*b–c*). The two shaded regions indicate the portion in (*a*) used for the time series shown in (*b–c*). The vorticity field and the corresponding spatial distribution of the inter-community in- and out-strengths between the pair of communities with the maximum inter-community interaction at each of the representative time instants marked in (*b–c*) are shown in (*d*). The red circles in (*d*) indicate the downstream convection of the coherent structure shed from the backward-facing step at the time instant (*ii*). The location of the community with the maximum outward influence matches with the location of the downstream moving coherent structure indicated with red circles during time instants (*ii–vii*). Subsequently, the coherent structure gets dissipated into the reaction field. The shedding and downstream convection of the coherent structure repeats during each acoustic cycle within the periodic epoch of intermittency and is reflected in the periodic nature of $A_{r,max}$ shown in (*c*).

ability of the network measure $A_{r,mean}$ to reflect the periodic spatio-temporal dynamics present in the reaction field during the periodic epoch of intermittency. However, we observe a significant correlation between the maximum of all inter-community interactions $A_{r,max}$ and the acoustic pressure fluctuations p' during the periodic epoch of intermittency.

One can observe the emergence of coherent structures shed from the backward-facing step during acoustic pressure minima (at time instant (*ii*) in figure 6*d*). This emergence of localised coherent spatial structures is suggestive of self-organisation in the reaction field (Mondal, Unni & Sujith 2017; George *et al.* 2018). The downstream convection of the coherent structure shed from the backward-facing step is indicated through red circles

https://doi.org/10.1017/jfm.2025.10362 Published online by Cambridge University Press

in figure 6(*d*). At the instant of the coherent structure shedding from the backward-facing step (shown at time instant (*ii*)), the regions of vortical communities with the maximum inter-community interaction do not match with the locations of the coherent structure shed from the backward-facing step. This is due to the coherent structure being present near the periphery of the spatial domain (adjacent to the backward-facing step), which results in low inter-community strength of the nodes belonging to the vortical communities that overlap with the recently shed coherent structure.

Subsequently, as the coherent structure shed from the backward-facing step convects downstream (time instants *ii–vii* in figure 6*d*), the inter-community interactions start to increase. Thus, the regions with vortical communities with maximum inter-community interactions match the regions of downstream convecting coherent structure until the acoustic pressure reaches the local maxima at the time instant (*vii*). Later, the coherent structure dissipates into the reactive flow field during the time instants marked (*viii–xi*). We again observe the shedding of a new coherent structure near the acoustic pressure minima at time instant (*xii*), and the above-discussed spatio-temporal dynamics continues for the next acoustic cycle during the periodic epoch of intermittency. This periodicity in vortical interactions that occur due to a periodic shedding and downstream convection of coherent structures during the periodic epoch of intermittency is reflected in the periodic time series of the network measure $A_{r,max}$, as seen in figure 6(*a*).

4.2.4. *Thermoacoustic instability*

Finally, in figure 7, we examine the spatio-temporal dynamics of maximum-interacting vortical communities over an acoustic pressure cycle during the state of thermoacoustic instability. Figures 7(*a*) and 7(*b*,*c*) show the time series of acoustic pressure fluctuations and network measures and their zoomed-in versions, respectively. Figure 7(*d*) shows the vorticity field and the corresponding pair of maximum-interacting communities in the spatial domain. The evolution of $A_{r,mean}$ and $A_{r,max}$ exhibits a significant periodic behaviour during the state of thermoacoustic instability. Unlike the results observed during the state of combustion noise, we notice large regions of spatially coherent vortical structures downstream of the backward-facing step during the state of thermoacoustic instability. Consequently, the vortical communities during the state of thermoacoustic instability are significantly less fragmented in the spatial domain compared with that observed during the state of combustion noise.

Notably, during the state of thermoacoustic instability, an almost consistent phase lag is present between the time instants when the coherent structures are shed from the backward-facing step (corresponding to the instants of local acoustic pressure p' minima) and the time instants when the vortical interactions have their maximum strength (local maxima of the network measures). This non-trivial phase lag contrasts our hypothesis that the vortical interactions will be maximum when the coherent structures are shed from the backward-facing step (during the local minima of p' oscillations) since the coherent structures start losing their strength as they convect downstream (Nair & Lieuwen 2007; Shanbhogue, Seelhorst & Lieuwen 2009). This phase lag arises since the interactions of the shed coherent structure with other coherent structures in the flow field do not depend simply on the vorticity of the nodes constituting the coherent structure but also on the distance of the coherent structure from other coherent structures. Although the coherent structure at the time of its shedding from the backward-facing step exhibits the most significant vorticity strength values, its considerable distance from other coherent structures in the flow field contributes to low vortical interactions. A decrease in this distance contributes to an increase in the magnitude of vortical interactions as the coherent

https://doi.org/10.1017/jfm.2025.10362 Published online by Cambridge University Press

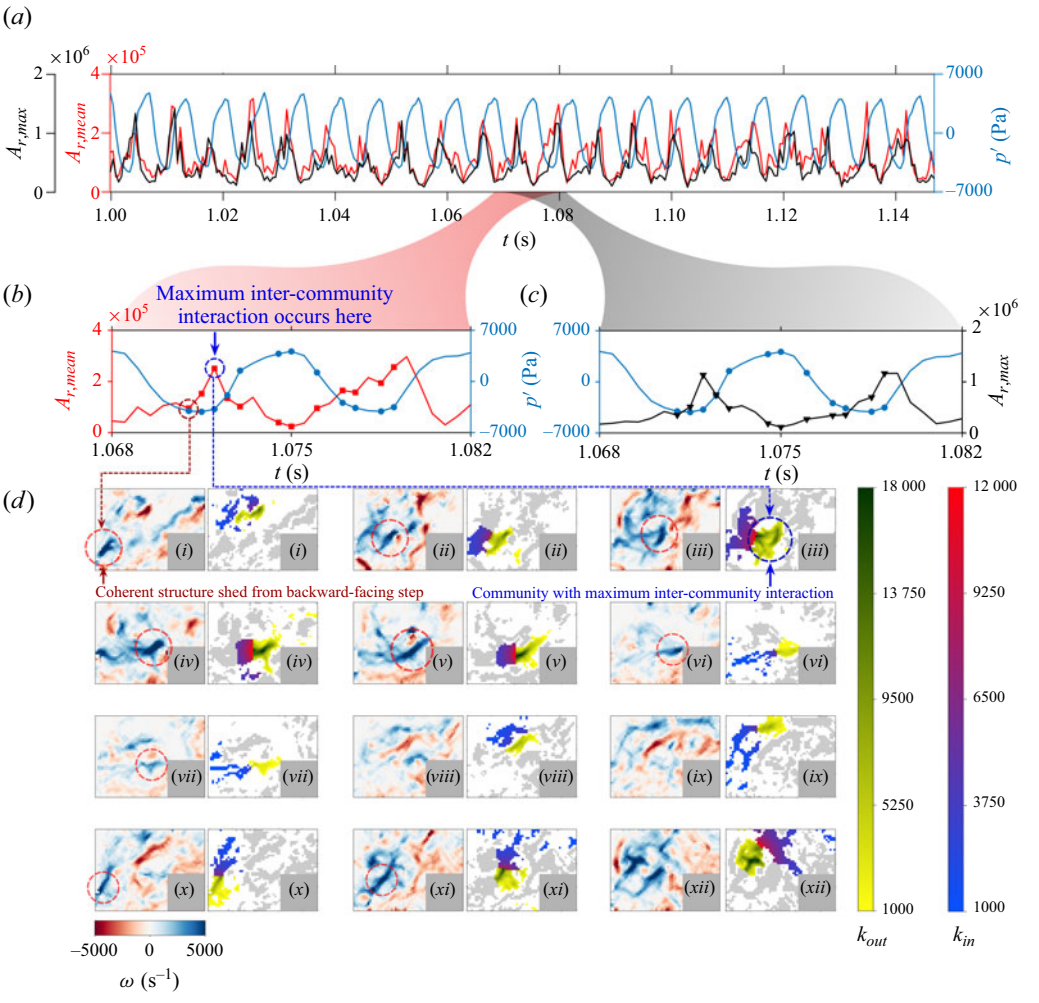


Figure 7. (*a*) Time series showing the variation of p' fluctuations and network measures (mean $A_{r,mean}$, and maximum $A_{r,max}$ of all inter-community interactions) during the state of thermoacoustic instability. The acoustic pressure fluctuations are marked in blue. The zoomed-in versions are shown in (*b–c*). The two shaded regions indicate the portion in (*a*) used for the time series shown in (*b–c*). The vorticity field and the corresponding spatial distribution of the inter-community in- and out-strengths between the pair of communities with the maximum inter-community interaction at each of the representative time instants marked in (*b–c*) are shown in (*d*). The red circles in (*d*) indicate the downstream convection of the coherent structure shed from the backward-facing step at the time instant (*i*). The coherent structure sheds from the backward-facing step at the time instant marked (*i*) in (*d*). However, the maximum inter-community interaction occurs at the time instant marked (*iii*) in (*d*). This phase lag between the time instants of vortex shedding and maximum inter-community interaction is approximately 51.42°. The location of the community with the maximum outward influence matches with the location of the downstream moving coherent structure indicated with red circles during the time instants (*i–vii*). Subsequently, the coherent structure gets dissipated into the reaction field. The shedding and downstream convection of the coherent structure repeats itself during each acoustic cycle present within the state of thermoacoustic instability and is reflected in the periodic nature of the network measures seen in (*b–c*).

https://doi.org/10.1017/jfm.2025.10362 Published online by Cambridge University Press

structure convects downstream towards the middle of the flow field. Subsequently, the loss of vorticity strength of the coherent structure dominates the small distance among different coherent structures, and the magnitude of vortical interactions decreases.

We can observe the above-mentioned behaviour by examining the spatio-temporal dynamics of the shedding of the coherent structure from the backward-facing step during the acoustic pressure minima (at time instant (*i*)) during the state of thermoacoustic instability. The downstream convection of the coherent structure shed from the backward-facing step at the minima of p' oscillations is indicated through red circles in figure 7(*d*). The regions of vortical communities with the maximum inter-community interaction match with the regions of coherent structure shed from the backward-facing step during the time instants (*ii–vii*). This matching of spatial regions of coherent structure shed from the backward-facing step and the community with maximum outward interaction is clearly visible till the acoustic pressure reaches the local maxima at the time instant (*vii*). Subsequently, as the coherent structure dissipates into the reactive flow field and the magnitude of vorticity present in the reactive field decreases during the time instants marked (*viii–ix*), it is difficult to discern the downstream movement of the coherent structure being discussed. We again observe the shedding of a new coherent structure near the acoustic pressure minima at time instant (*x*), and the above-discussed spatio-temporal dynamics continues for the next acoustic cycle.

As mentioned above, one can expect the vortical interactions in the combustor to be maximum at the instant of shedding as the shed vortices lose their strength via dissipation to the surroundings during their convection downstream. However, we observe a lag between the occurrences of vortex shedding and maximum vortical interactions in figure 7(*a*). In figure 7(*b*), this phase lag can be observed between the time instants marked (*i*) and (*iii*) in figure 7(*d*). We notice the newly formed coherent structure shedding from the backward-facing step at the acoustic pressure minima marked 1 in figure 7(*b*). However, the maximum inter-community interaction occurs at the time instant marked 3. To calculate the phase difference between points (i) and (iii), we consider the fact that there are 14–16 points with velocity fields obtained from 2C PIV measurements in an acoustic pressure cycle during the state of thermoacoustic instability. Thus, the phase lag between two adjacent 2C PIV data points varies between $360°/(16-1) = 24°$ and $360°/(14-1) = 27.69°$. Since the time instants of vortex shedding and maximum inter-community interaction occur at points marked 1 and 3 in figure 7(*b*), the phase lag between these two points is approximately in the range of $24° \times 2 = 48°$ to $27.69° \times 2 = 55.38°$.

To perform the above phase lag analysis for the entire time series of p' and $A_{r,max}$ corresponding to the state of thermoacoustic instability, we use cross-correlation between the time series of p' fluctuations and $A_{r,max}$ to compute the phase lag between the vortex shedding and the occurrence of maximum vortical interactions. The minima of p' fluctuations correspond to the instants of vortex shedding. A few representative instants of phase lags and the cross-correlation ($r_{p'A_{r,max}}$) are shown in figures 8(*a*) and 8(*b*), respectively. The minima of cross-correlation closest to 0° in figure 8(*b*) indicates the phase lag where p' and $A_{r,max}$ are maximum negatively correlated. We consider maximum negative correlation since the minima of p' fluctuations and maxima of $A_{r,max}$ are used for computing the cross-correlation. We observe that a significant phase lag of about 51° is present between the instants of vortex shedding from the backward-facing step and the maximum inter-community interactions.

The discrepancy between the phase-averaged regions of vorticity and participation coefficient, as discussed in § 4.1, can now be understood by interpreting the phase lag mentioned in the previous paragraph. The region of maximum outward inter-community interaction is located between the backward-facing step and the centre of the flow

https://doi.org/10.1017/jfm.2025.10362 Published online by Cambridge University Press

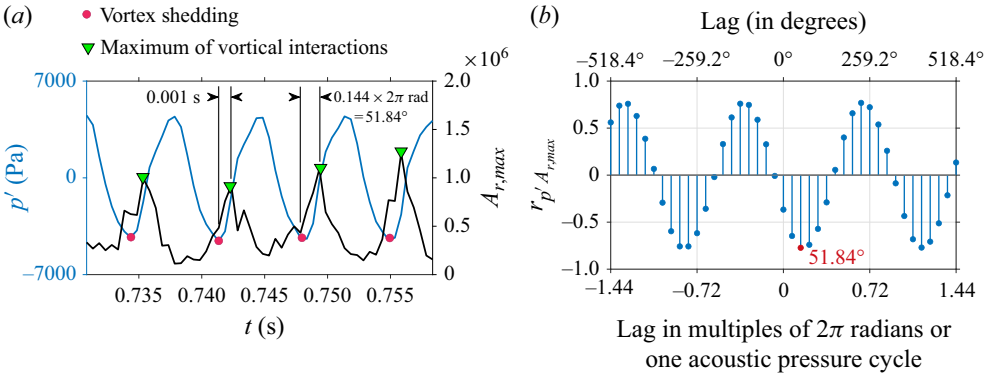


Figure 8. (*a*) Time series of p' fluctuations and $A_{r,max}$, indicating the instants of vortex shedding and maximum vortical interactions through red circles and green triangles, respectively. (*b*) Shows the cross-correlation between p' and $A_{r,max}$, denoted by $r_{p'A_{r,max}}$ and the corresponding lags in terms of multiples of acoustic pressure cycles (2π rad is equivalent to one acoustic pressure cycle) and degrees. The minima of $r_{p'A_{r,max}}$ is at 52°, indicating the lag between the occurrences of p' minima (i.e. vortex shedding from the backward-facing step) and maximum of vortical interactions.

field. Considering the phase angle, where 0° marks the instant a vortex is shed at the upstream backward-facing step (cf. figure 3*a*), an increase in phase angle corresponds to the downstream convection of the shed vortex, as shown in figure 3(*c*). Furthermore, figure 3(*b*) shows that the region of maximum outward inter-community interaction corresponds to a phase angle of approximately 45°. This is very close to the phase lag of 52° mentioned in the previous paragraph. Thus, even as the vortex shed from the backward-facing step continues to move downstream, the region of maximum outward inter-community interaction remains around 52°, explaining the observed discrepancy between the phase-averaged regions of vorticity and participation coefficient. This shows that in addition to the crucial role coherent structures play in combustion systems, the interaction of vortical elements is also necessary to comprehensively understand the flow physics in combustion systems.

4.3. *Insights into critical region detected for open-loop control*

Having analysed the spatio-temporal evolution of maximum-interacting pairs of communities during different dynamical states exhibited by the turbulent combustor, we now focus on the relevance of maximum inter-community interactions toward mitigating thermoacoustic instability. The turbulent combustor being discussed in the current study exhibits vortex-driven thermoacoustic instability. Thus, the mitigation of thermoacoustic instability in this type of combustor is intricately related to leveraging our understanding of the vortex-driven spatio-temporal dynamics. Open-loop control strategies are widely used in practical combustion systems due to their minimal maintenance requirements and high durability. One of the open-loop control methods is to target certain critical regions using secondary fuel or air to perturb the flow regions responsible for controlling the overall dynamics of the system. Ghoniem *et al.* (2005) and co-workers (Altay *et al.* 2007, 2010) determined the optimum region as the region of flame anchoring and considered a steady injection of secondary air for achieving control in a dump combustor. Uhm & Acharya (2005) considered the region of local maxima in the heat release rate field to be the critical region. In a similar study, Tachibana *et al.* (2007) optimised the secondary fuel injector parameters using the Rayleigh Index distribution to control thermoacoustic instability in a swirl-stabilised lean premixed combustor actively.

https://doi.org/10.1017/jfm.2025.10362 Published online by Cambridge University Press

The first step toward suppressing thermoacoustic instability is to heuristically find the critical region where the secondary injection to achieve open-loop control should be targeted. The high correlation between network measures and acoustic pressure fluctuations during the state of thermoacoustic instability, as seen in figure 7, motivates us to conjecture that communities with maximum inter-community interactions play a critical role towards the macroscopic dynamics exhibited by the combustor. Disrupting the interactions between the communities having the maximum interaction during thermoacoustic instability can help us to break the positive coupling between the vortical interactions and acoustics in the combustor, thus suppressing the high-amplitude acoustic pressure fluctuations. This would, in turn, correspond to perturbing the closely positioned regions of high vorticity that are detected as the largest interacting pair of communities in the network space. While the results suggest that targeting these regions may help disrupt the positive coupling between vortical interactions and acoustics in the combustor, it is important to note that further rigorous causal analysis can be carried out to quantitatively establish a correlation between the injector locations and the suppression of thermoacoustic instability

Thus, our final objective is to understand the occurrence of the critical regions in the reaction flow field through the lens of vortical interactions analysed via complex networks. To this end, we plot the spatial distribution of vortical communities having the maximum interaction (at all time instants) during the states of combustion noise, intermittency and thermoacoustic instability in figure 9(*ai–iii*). For each dynamical state, 3796 snapshots (equivalent to 300 acoustic cycles present during the state of thermoacoustic instability) are utilised for this analysis. The spatial distribution of the communities having maximum interaction is plotted by first detecting the pair of such communities at each time instant during a dynamical state. All such pairs of communities having the maximum inter-community interactions at all the time instants are subsequently overlapped in the spatial domain to identify the region where such influential communities are most likely to be found. The colour bar for figure 9(*a*) represents the number of vortical communities with maximum inter-community interactions detected during the three different dynamical states. We also plot the spatial distribution of weights of the maximum inter-community interactions in figure 9(*b*), where we plot the corresponding kernel smoothed intensity function of $A_{r,max}$. Here, $A_{r,max}$ is the magnitude of the largest inter-community interaction and is equal to the largest element of the reduced adjacency matrix.

In figure 9(*a*,*b-i*), we observe that the influential communities are present primarily above the bluff body during the state of combustion noise. These vortical communities correspond to the small-sized clockwise vortices shed from the tip of the bluff body due to the flow turning at the corner of the bluff body. We also detect a distinct region with maximum-interacting vortical communities downstream of the backward-facing step during the state of intermittency figure 9(*a*,*b-ii*). The periodic and the aperiodic epochs are considered together while calculating the region of the maximum-interacting pair of interactions during the state of intermittency. The vortices are shed almost periodically at the backward-facing step for short epochs of time during the periodic epoch of intermittency, after which they may break down into smaller vortices or impinge on the walls of the combustor or bluff body. The location of this region is consistent with the critical regions detected during the state of intermittency by plotting quantities such as Hurst exponent and the node strengths of the $p'\dot{q}'$-ω multilayer network, as seen in Roy *et al.* (2021) and Tandon & Sujith (2023), respectively. Other physical measures such as the Fourier amplitude of turbulent velocity fluctuations (Roy *et al.* 2021), weighted closeness centrality in a weighted spatial correlation network obtained from the velocity field in Krishnan *et al.* (2019*a*) and node strength of the phase-averaged vortical network

https://doi.org/10.1017/jfm.2025.10362 Published online by Cambridge University Press

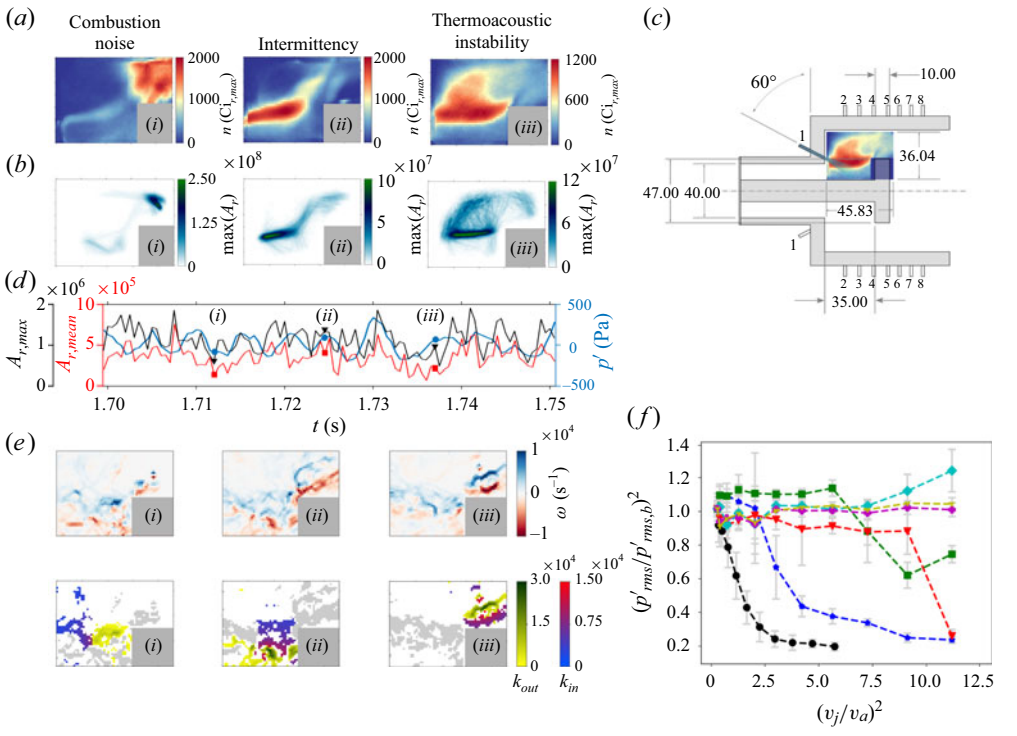


Figure 9. (*a*) The distribution of the spatial location of vortical communities with the maximum inter-community interactions during the states of combustion noise, intermittency and thermoacoustic instability. Here, $n(\mathrm{Ci}_{r,max})$ denotes the number of overlapped vortical communities used to plot the distribution of the spatial location of vortical communities with the maximum inter-community interactions. (*b*) Plot of kernel smoothed intensity function of the maximum inter-community interactions. Consistent with the results discussed in figure 4(*d*), most of the communities with maximum inter-community interactions are present above the bluff body during the state of combustion noise. (*c*) Shows the cross-section of the combustion chamber showing the microjet injector locations. (*d*) Shows the aperiodic network measures and the p' fluctuations during the state of suppression of thermoacoustic instability when air microjet is injected through injector number 1. (*e*) Shows the spatio-temporal variation of vorticity and regions of maximum inter-community interaction during the state of suppression. (*f*) Is adapted with permission from Krishnan *et al.* (2021) and shows the variation of normalised root-mean-square values of p' due to air microjet injection at different locations shown in (*c*). The horizontal axis shows the total momentum flux ratio of the air microjet. The vertical error bars denote the standard deviation. The air microjet injected via port 1 induces the most efficient suppression of thermoacoustic instability with the least momentum flux ratio of the air microjet. (*c*) Illustrates how air microjet injection via port 1 appears to disrupt the region with maximum inter-community interactions during the state of thermoacoustic instability. While the disruption may not be significant, some degree of correlation can be observed between disruption of the region of maximum inter-community interaction and suppression of thermoacoustic instability.

(Krishnan *et al.* 2021) can identify critical region only during the state of thermoacoustic instability, not during intermittency.

Finally, during thermoacoustic instability, the region with maximum-interacting vortical communities increases in size and extends from the backward-facing step to the upstream boundary of the bluff body, as seen in figure 9(*a*,*b-iii*). A significant part of this critical region, calculated through the present methodology during the state of thermoacoustic instability, is consistent with the corresponding critical regions detected through the spatial distribution of Hurst exponent (cf. figure 9*c* in Roy *et al.* 2021), weighted closeness centrality of weighted spatial correlation networks constructed from velocity field

https://doi.org/10.1017/jfm.2025.10362 Published online by Cambridge University Press

(cf. figure 1*c* in Krishnan *et al.* 2019*a*) and node strength of the phase-averaged vortical network (cf. figure 13*b* in Krishnan *et al.* 2021). The consistency of the region having maximum-interacting vortical communities detected in the current study with that of critical regions detected in previous studies provides strong evidence that the community-based formulation can effectively capture critical regions in reactive flow systems and shed light on the spatio-temporal dynamics of vortex-driven thermoacoustic systems.

Open-loop control requires knowledge about the relative importance of different regions in the flow field. In the experimental set-up used in the present study, Krishnan *et al.* (2021) introduced microjets of air into the critical region to suppress thermoacoustic instability. Microjets of air steadily injected through the injector numbered 1 (cf. figure 9*c*) resulted in the most efficient mitigation of thermoacoustic instability compared with injection via other ports. We conjecture that this targeted control disrupted the key vortical communities with the maximum inter-community interactions present during the state of thermoacoustic instability, thus mitigating instability. During the state of suppression of thermoacoustic instability through microjet injection via injector 1, we observe in figure 9(*d*) that the time series of the mean ($A_{r,mean}$) and maximum ($A_{r,max}$) of all inter-community interactions exhibit an aperiodic dynamics, similar to that present in the time series of acoustic pressure fluctuations. The aperiodic dynamics exhibited by the network measures is similar to that observed during the state of combustion noise shown in figure 4(*a*). Figure 9(*e*) shows the snapshots of vorticity distribution and inter-community node strengths of the pair of communities with the largest inter-community interaction. Amongst all the air microjet injection ports shown in figure 9*c*), injecting air through port 1 leads to the maximum suppression of thermoacoustic instability (figure 9*f*).

While the data presented in figure 9(*f*) demonstrate a correlation between microjet injector placement and suppression efficiency, it should be noted that the current analysis does not quantitatively establish the optimality of this placement through a causal investigation. The observed suppression bears a noticeable correlation with the disruption of key vortical communities identified through vortical network analysis. However, further studies involving a more comprehensive quantitative approach are required to investigate these findings. For instance, a network dynamical system could be developed by examining the impact of perturbing specific spatial locations (network nodes) using microjets of air, with the perturbations modelled as varying magnitudes of external disturbances applied to the network.

5. Concluding remarks

A great deal of previous research into thermoacoustic instability has focused on the role of coherent structures in driving thermoacoustic instability in turbulent combustors. Rogers & Marble (1956) provided the earliest description of the role of vortices in thermoacoustic instability. They showed that a transverse acoustic mode excited in an acoustic duct triggered the shedding of vortices in the reaction field. Subsequently, a significant portion of the work done since the 1980s has extended our knowledge of understanding how coherent structures contribute to thermoacoustic instability (Smith & Zukoski 1985; Poinsot *et al.* 1987; Hussain, Jamshed & Ozair 2022).

However, several questions remain unanswered on the dynamics of the interaction of vortical structures in turbulent thermoacoustic systems. This paper argues that, in contrast to the hypothesis that vortical interactions will be close to the instants of shedding of coherent structure (Nair & Lieuwen 2007; Shanbhogue *et al.* 2009), these interactions attain their maxima downstream in the flow field. To show this, we compute the critical interactions between regions of intense vorticity through induced velocities calculated

https://doi.org/10.1017/jfm.2025.10362 Published online by Cambridge University Press

using the Biot–Savart Law. These induced velocities are used to construct time-varying weighted directed networks, termed vortical networks. The vortical networks are used to identify the communities or modular structures in the unsteady flows through the modularity maximisation algorithm. The temporal variation of the vortical interactions is captured via the time series of mean and maximum inter-community interactions. Subsequently, we show a consistent phase lag between the instants of shedding of coherent structures during the state of thermoacoustic instability and the instants where the vortical interactions achieve their maximum value. The strong delayed correlations observed between the statistics of vortical community interactions and the acoustic pressure fluctuations during the state of thermoacoustic instability emboldens us to conjecture that the key vortical community interactions play a critical role in the behaviour exhibited by the combustor. Taking a cue from this line of thought, we also show that the regions exhibiting the largest inter-community interactions are consistent with the critical regions detected during the states of intermittency and thermoacoustic instability in previous studies. Perturbing the regions of the most influential pair of communities disrupts the largest inter-community interactions in a temporally averaged manner and leads to the maximum suppression of thermoacoustic instability. Our results complement the findings in earlier works by Krishnan *et al.* (2019*a*), Roy *et al.* (2021), Krishnan *et al.* (2021), Tandon & Sujith (2023) and Premchand *et al.* (2024) on the same experimental set-up, thus validating our approach.

While acknowledging the limitations inherent in our study due to the discrepancy between the actual three-dimensional flow field and the two-dimensional data acquired, we are hopeful that our work effectively elucidates the relevant physics of the complex flow field of a turbulent thermoacoustic system. Our optimism stems from the fact that the significant features of the turbulent flow field, such as the periodic shedding of vortices during the states of periodic epochs of intermittency and thermoacoustic instability, are adequately captured in the two-dimensional PIV data. Moreover, the two-dimensional PIV data capture irregular spatio-temporal behaviour of the flow field during the states of combustion noise and aperiodic epochs of intermittency, consistent with our understanding of these dynamical states. Nevertheless, we recognise that three-dimensional simulations or three-component tomographic PIV can potentially reveal additional information that our current two-dimensional PIV data cannot fully capture. Future studies incorporating three-dimensional experimental and computational data can complement and extend our findings, providing a more comprehensive understanding of vortical interactions in turbulent reactive flow fields. Furthermore, baroclinic torque and dilatation have been proven to play a pivotal role in the vorticity dynamics of reactive flow fields (Geikie & Ahmed 2018; Geikie *et al.* 2021; Rising *et al.* 2021). We look forward to future work utilising three-dimensional stereoscopic PIV and Mie scattering data, acquired at a sufficiently high sampling rate, to investigate the role of different vorticity generating mechanisms in the dynamics of vortical interactions in turbulent combustors.

In closing, the current method has the potential for widespread application in combustion and other fluid-mechanical systems. First, it enables us to recognise and quantify how the interactions between different vortical communities correlate with the macroscopic dynamics exhibited by the fluid-mechanical systems. In addition to the already well-established role of coherent structures in combustion systems, analysing the interaction between different vortical elements is essential to understanding the spatio-temporal dynamics of combustion systems. Secondly, for combustion systems susceptible to thermoacoustic instability, the distribution of vital vortical communities during the state of intermittency can be used to explain the occurrence of critical regions that have been

https://doi.org/10.1017/jfm.2025.10362 Published online by Cambridge University Press

shown to drive thermoacoustic instability. Thirdly, the present work provides a potential way forward to develop low-order models for a turbulent thermoacoustic system using the statistical behaviour of communities, the inter- and intra-community strengths and the locations of communities in the reactive field of the combustor. Finally, the present methodology provides a path for the future development of advanced flow control efforts to alter the dynamics of vortical structures in turbulent fluid-mechanical systems. The present methodology is generalisable to arbitrary thermofluid systems where instability control is crucial.

Acknowledgements. We thank J.M. Dhadphale, S. Singh and G. Chopra for countless fruitful discussions. We acknowledge Thilagaraj S., A. Selvam, M. Raghunathan and A. Krishnan for providing the experimental data. A.S. is grateful to the Ministry of Education for the Half-Time Research Assistantship (HTRA). The authors are grateful to Professor K. Taira for fruitful discussions.

Notice: This manuscript has been authored in part by UT-Battelle, LLC, under contract DE-AC05-00OR22725 with the US Department of Energy (DOE). The US government retains and the publisher, by accepting the article for publication, acknowledges that the US government retains a nonexclusive, paid-up, irrevocable, worldwide license to publish or reproduce the published form of this manuscript, or allow others to do so, for US government purposes. DOE will provide public access to these results of federally sponsored research in accordance with the DOE Public Access Plan (https://energy.gov/downloads/doe-public-access-plan).

Funding. R.I.S. is grateful for the funding from the Office of Naval Research Global (Grant No. N62909-18-1-2061; Funder ID: 10.13039/100007297), and the Institute of Eminence (IoE) initiative of IIT Madras (SB/2021/0845/AE/MHRD/002696). This research used resources of the Oak Ridge Leadership Computing Facility at the Oak Ridge National Laboratory, which is supported by the Office of Science of the US Department of Energy under Contract No. DE-AC05-00OR22725.

Declaration of interests. The authors report no conflict of interest.

Data availability statement. The data that support the findings of this study are available from the corresponding author upon reasonable request.

Appendix A. Vorticity thresholding

We use vorticity thresholding to utilise fluid elements with sufficiently high vorticity magnitudes for vortical community detection. For each time instant, we calculate the range of vorticity values $\omega \in [\omega_-, \omega_+]$ that contribute to a lower range of 10 % of the total circulation Γ present in the reaction field at that time instant (for instance, $\Gamma_{th} = 10\,\% = 0.1 \times \Gamma$). Finally, we compute the average of all the vorticity thresholds calculated for this circulation threshold, i.e. $\overline{\omega}_- = (1/N) \sum \omega_-$ and $\overline{\omega}_+ = (1/N) \sum \omega_+$. We repeat the above procedure removing different lower ranges of the total circulation, i.e. 20 %, 30 %, . . . , 90 %. We plot the corresponding vorticity threshold values in figure 10(*a*). Here, $N = 3796$ is the total number of snapshots of temporal vorticity fields available for each dynamical state.

The fluid elements with vorticity outside the aforementioned interval, i.e. the fluid elements with $\omega \notin [\omega_-, \omega_+]$, are subsequently used to calculate the vortical communities at each time step. The area occupied by all the vortical communities for a circulation threshold Γ_{th} is denoted by A_{th}. The average of A_{th} calculated at all the time instants, i.e. $\overline{A}_{th} = (1/N) \sum A_{th}$, is plotted in figure 10(*b*) as a fraction of the total area of the spatial domain.

The vorticity values corresponding to the lower range of 20 % of the total circulation are used for vorticity thresholding in the current study. The threshold values are highlighted with green background in figure 10(*a*), and are equal to $|\omega| = 456$, 380, 843 and 532 s^{-1} during the states of combustion noise, intermittency, thermoacoustic instability

https://doi.org/10.1017/jfm.2025.10362 Published online by Cambridge University Press

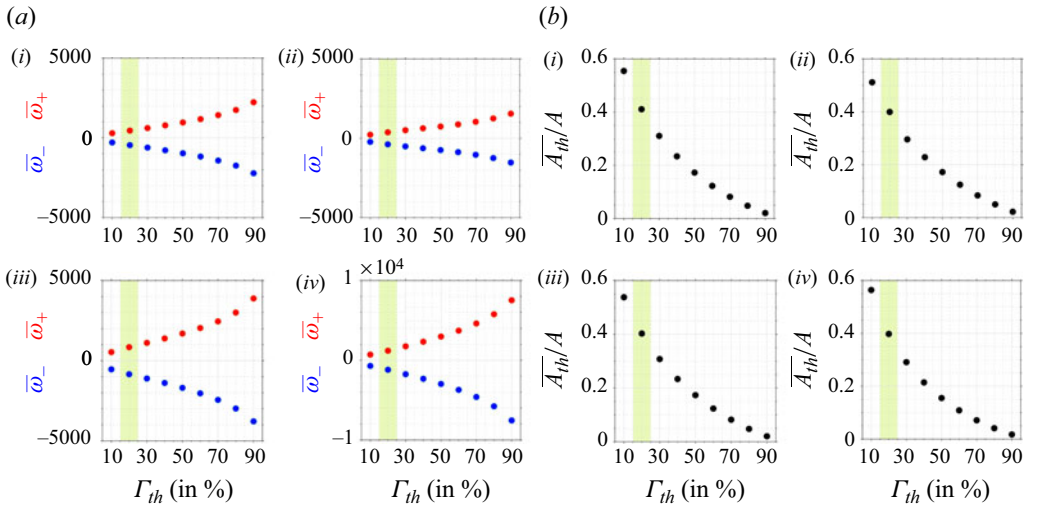


Figure 10. (*a*) Variation of mean positive ($\overline{\omega}_+$) and mean negative ($\overline{\omega}_-$) vorticity threshold values with respect to the total circulation threshold (Γ_{th} in %) for the states of (i) combustion noise, (ii) intermittency, (iii) thermoacoustic instability and (iv) suppression through air microjet injection. The fluid elements with vorticity $\omega \in [\overline{\omega}_-, \overline{\omega}_+]$ are disregarded to exclude the bottom Γ_{th} % of the total circulation present in the reaction field, thus capturing the influential regions of the flow. The $\overline{\omega}_+$ and $\overline{\omega}_-$ values present on the green band are subsequently used as thresholds while using the Louvain algorithm to detect vortical communities. (*b*) Variation of the mean area percentage of the reaction field $\overline{A}_{th}$ occupied by the vortical communities. We do not consider the area of the bluff body mask while calculating the percentage with respect to the total area of the reaction field. For all the cases, the resolution parameter γ used in the Louvain algorithm is kept consistent at 1 (Gopalakrishnan Meena *et al.* 2018; Gopalakrishnan Meena & Taira 2021).

and microjet injection, respectively. The robustness of the thresholds is evaluated by noting that the qualitative results do not change significantly even if the threshold values are modified in $\pm 50\ \mathrm{s}^{-1}$ range around the values considered in the current study. Approximately 40 % of the area of the reaction field considered in the current study is occupied by the detected vortical communities during all the dynamical states.

Appendix B. The Louvain algorithm and its non-deterministic nature

Community detection algorithms are widely employed to bring out the underlying mesoscopic structure, thereby revealing the clustered nature of complex networks. While there is no formal definition for the concept of communities, the idea is to group nodes into distinct, densely connected parts, with the density between parts being low. Researchers continue to develop scalable methods to reveal densely connected groups due to the constant rise in data and dimensions. Due to the efficiency of their implementation, algorithms that maximise modularity have garnered considerable attention. Newman (2004) created modularity as a quality function to assess the quality of a partition as a community structure. It compares the existence of an edge within a community with the probability of having such an edge between corresponding vertices in a random network with the same degree distribution. While it is known that modularity has some limitations (Fortunato & Barthelemy 2007; Lancichinetti & Fortunato 2011), heuristic-based algorithms that maximise this measure remain the most effective on large networks to this day (Blondel *et al.* 2008; Leicht & Newman 2008). The Louvain algorithm is one of the most popular algorithms used to maximise modularity (Blondel *et al.* 2008).

https://doi.org/10.1017/jfm.2025.10362 Published online by Cambridge University Press

The Louvain algorithm begins by creating communities of size one, where each node in the network forms a community. The algorithm then proceeds by executing two stages. The algorithm assigns a node i to a community of a neighbour j to increase the partition's modularity in the first stage. The first stage is repeated until the modularity cannot be increased. This procedure generates an initial network partition. In the second stage of the Louvain algorithm, each partition's community is considered a supernode. If at least one edge exists between nodes of each community that the supernode represents, then the supernodes are connected. After this second stage is completed, the algorithm iterates until the modularity can no longer increase.

The Louvain algorithm is non-deterministic due to the changes in the following two steps between different runs: (i) the order in which all the nodes are processed and (ii) the order in which two pairs of nodes are assigned to two different communities if the increase in modularity is equal for both the assignments (Cordeiro, Sarmento & Gama 2016). Thus, the community affiliations may vary between different implementations of the Louvain algorithm even when the exact same data set is used.

To evaluate the extent of consistency between community structures obtained from different implementations of the Louvain algorithm on the same vortical network, we implement the Louvain algorithm 100 times at each time instant and calculate the following quantities for all the vortical networks corresponding to all the time instants:

(i) Coefficient of variation of modularity, $\sigma(M)/\overline{M}$, obtained from a hundred different community affiliations at each time instant. The coefficient of variation is the ratio of the standard deviation to the mean of the modularity values obtained from different runs of the Louvain algorithm and shows the extent of variability with respect to the mean of the modularity values (Castagliola *et al.* 2013). The higher the coefficient of variation is, the greater the difference between the modularity values obtained between different implementations of the Louvain algorithm on the same vortical network.

(ii) Coefficient of variation of the number of communities obtained from 100 different community affiliations at each time instant.

(iii) Maximum of normalised variation of information (NVI) to indicate the maximum deviation between any two community affiliations out of 100 different implementations of the Louvain algorithm for each time instant (Meilă 2007; Karrer, Levina & Newman 2008). The NVI between two community affiliations X and Y is given by

$$NVI(X, Y) = -\sum_{ij} r_{ij}\left[\log\left(\frac{r_{ij}}{p_i}\right) + \log\left(\frac{r_{ij}}{q_j}\right)\right], \tag{B1}$$

where

$$p_i = \frac{|X_i|}{n,\, q_j} = \frac{|Y_j|}{n,\, r_{ij}} = \frac{|X_i \cap Y_j|}{n,\, n} = \sum_i |X_i| = \sum_j |Y_j|. \tag{B2}$$

An NVI equal to one indicates the maximum difference between two clustering of the same complex network, which occurs when each node is assigned to its own community in one clustering, and the entire network is assigned to one single community in the other clustering.

https://doi.org/10.1017/jfm.2025.10362 Published online by Cambridge University Press

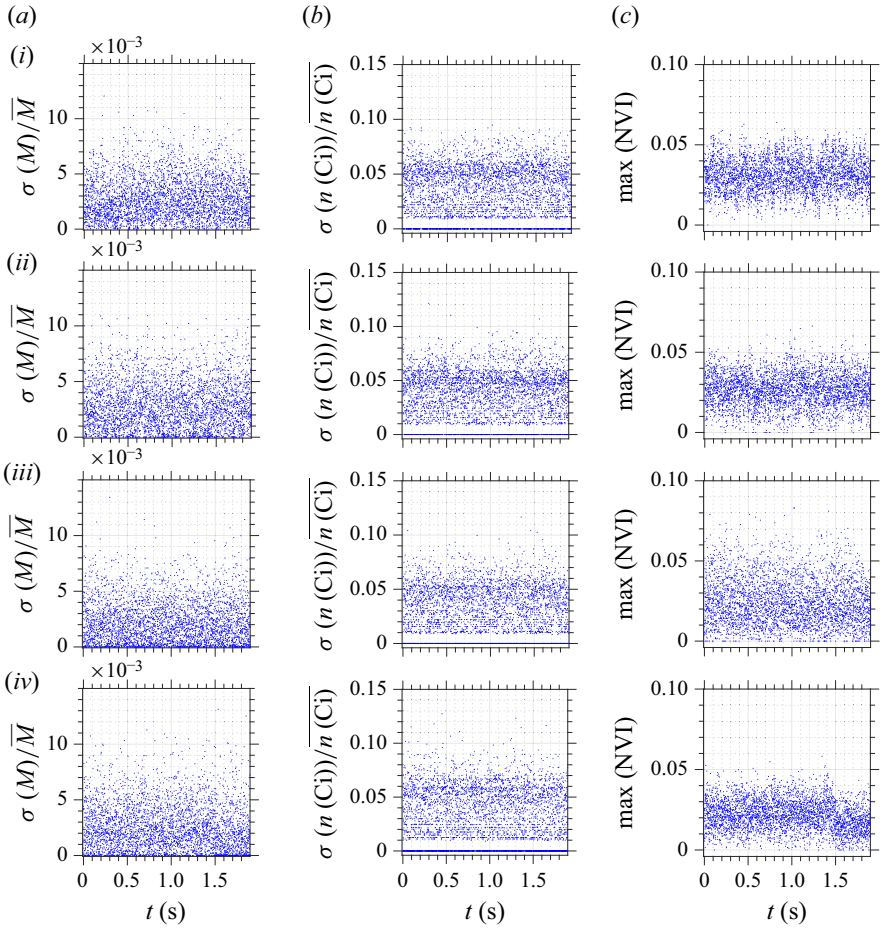


Figure 11. (*a*) Plot of the standard deviation of modularity values, (*b*) coefficient of variation of the number of communities and (*c*) maximum normalised variation of information calculated through 100 implementations of the Louvain algorithm at each time instant during the states of (*i*) combustion noise, (*ii*) intermittency, (*iii*) thermoacoustic instability and (*iv*) suppression of thermoacoustic instability through air microjet injection.

In figure 11, we observe that the three aforementioned quantities calculated are quite low for all four dynamical states, indicating that different implementations of the Louvain algorithm give us statistically similar community affiliations for a dataset.

Appendix C. Spatial coherence of vortical communities

In figure 5, we observe that the communities detected during the state of combustion noise are highly fragmented in comparison with the communities detected during the other two dynamical states of intermittency and thermoacoustic instability. The highly fragmented communities present during the state of combustion noise are associated with the chaotic spatiotemporal dynamics observed in the reaction field. Furthermore, most of the pairs of communities with the maximum inter-community interactions are present above the bluff body and their spatial locations match with the coherent structures shed from the upstream tip of the bluff body. On the other hand, most of the highly interacting communities observed during the states of intermittency and thermoacoustic instability match with the locations of coherent structures shed from the backward-facing step.

https://doi.org/10.1017/jfm.2025.10362 Published online by Cambridge University Press

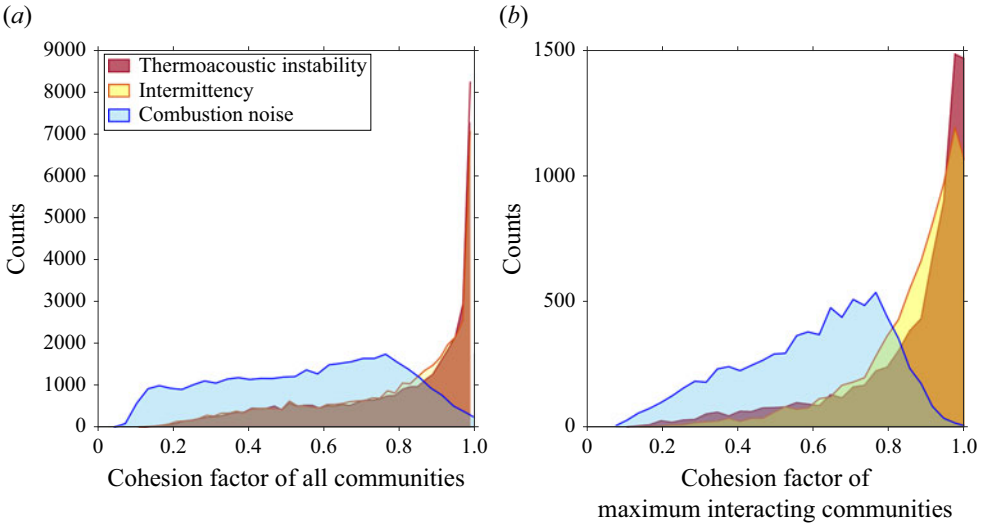


Figure 12. Distributions of cohesion factor indicating the spatial coherence of (*a*) all vortical communities and (*b*) vortical communities with maximum inter-community interactions during the three dynamical states.

To quantify the extent of fragmentation of vortical communities during the three dynamical states, we adopt a measure used by Jadhav, Guttal & Masila (2022) that measures the size of the largest 4-connected cluster in any detected community normalised by the total size of the community. This measure is called the cohesion factor. A cohesion factor equal to one implies that the communities are 4-connected everywhere, with no fragmentation at all. A cohesion factor of zero indicates an absence of any connected component.

In figure 12, we plot the distributions of the cohesion factors of all the vortical communities and of the maximum-interacting vortical communities during the three dynamical states. We notice that the cohesion factors of the communities during the state of combustion noise are comparatively low compared with the cohesion factors observed during the other dynamical states of intermittency and thermoacoustic instability. The highly fragmented nature of vortical communities detected during the state of combustion noise can be attributed to the presence of very few small vortices scattered throughout the spatial domain. Moreover, the fragmented nature of maximum-interacting vortical communities is due to the small coherent structures primarily shed from the tip of the bluff body during the state of combustion noise.

During the states of intermittency and thermoacoustic instability, most of the coherent structures are shed from the backward-facing step. Since these coherent structures are highly organised in the spatial domain, the vortical communities detected during these states are comparatively less fragmented than those present during the state of combustion noise. Thus, the cohesion factors of the vortical communities present during the states of intermittency and thermoacoustic instability are quite high and very close to 1.

Appendix D. Sensitivity of community detection and associated results to α values

We set $\alpha = 0$ to account for directed interactions between vortical elements. Choosing $\alpha = 1$ would yield similar results, as defining $u_{i\to j}$ as A_{ij} or A_{ji} is a matter of convention. In our formulation, we use $\alpha = 0$ to follow the convention of denoting $u_{i\to j}$ as A_{ji}, which is consistent with studies in physical sciences. The same notation is followed in Newman (2018).

https://doi.org/10.1017/jfm.2025.10362 Published online by Cambridge University Press

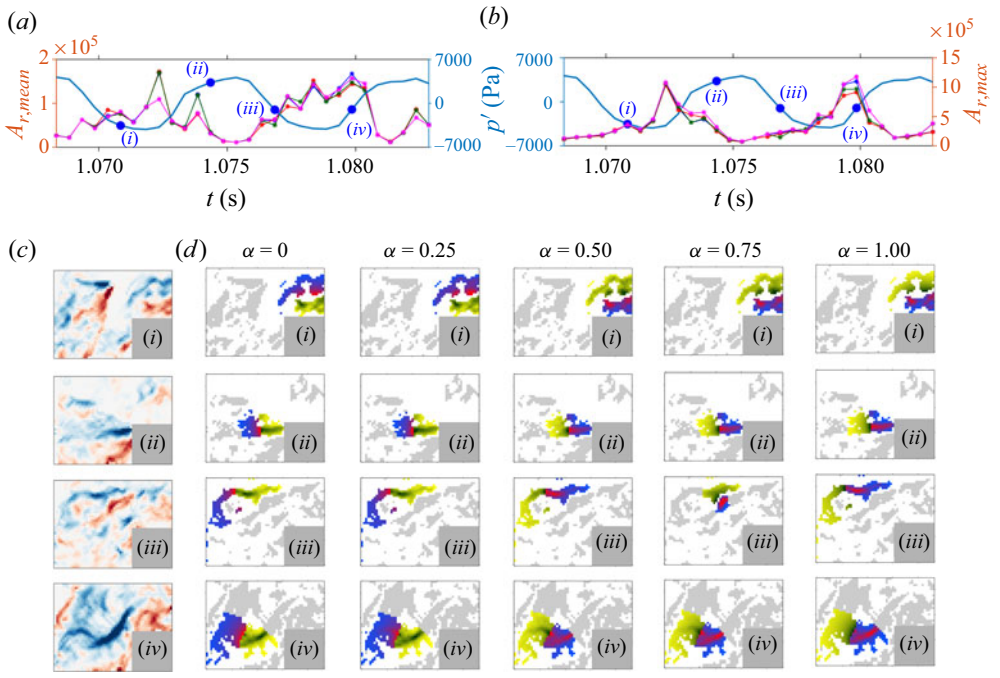


Figure 13. Time series showing the variation of the (*a*) mean ($A_{r,mean}$) and (*b*) maximum ($A_{r,max}$) of all inter-community interactions during the state of thermoacoustic instability. The acoustic pressure fluctuations are shown in blue, and the inter-community interaction measures are marked with star-shaped markers. Five different values of $\alpha = 0$, 0.25, 0.5, 0.75 and 1.00 are used to plot $A_{r,mean}$ and $A_{r,max}$ in (*a*) and (*b*). The results indicate that the inter-community interaction measures $A_{r,mean}$ and $A_{r,max}$ do not change significantly with variations in α. (*c*) Shows the vorticity fields corresponding to the four data points marked *i*–*iv* in (*a*) and (*b*). For these data points, each column in (*d*) illustrates the locations and strength distributions of the communities with the largest inter-community interaction for different values of α. The pair of communities with the largest inter-community interaction remains consistent as α changes. However, the direction of links between the two communities reverses as α transitions from 0 to 1. This reversal is evident from the opposite colour schemes of the communities with in-degrees and out-degrees for $\alpha = 0$ and 1.

The sensitivity of the results to unidirectional coupling (parameterised by α) can be explained by studying the impact of α on the following aspects of vortical networks:

D.1. *Community affiliations*

To study the sensitivity of results to changes in the values of α, we calculate inter-community interactions, community affiliations and sizes of the communities with maximum inter-community interactions for five different values of α – 0, 0.25, 0.50, 0.75 and 1.00.

In figure 13(*a*,*b*), the time series with star markers show the variation of the mean ($A_{r,mean}$) and maximum ($A_{r,max}$) of inter-community interactions for the different values of α during the state of thermoacoustic instability. Changing the α values modifies the induced velocities between vortical elements. However, this modification occurs uniformly across all pairs of nodes. Thus, the location of local maxima of network measures does not change significantly as seen in figure 13(*a*,*b*), although we do observe slight changes in the magnitudes of $A_{r,mean}$ and $A_{r,max}$.

To study the effect of α on the spatio-temporal dynamics of the maximum-interacting pair of communities, we plot the locations of the pair of communities with maximum inter-community interactions for four different data points marked (*i*)–(*iv*) in figure 13(*a*,*b*).

https://doi.org/10.1017/jfm.2025.10362 Published online by Cambridge University Press

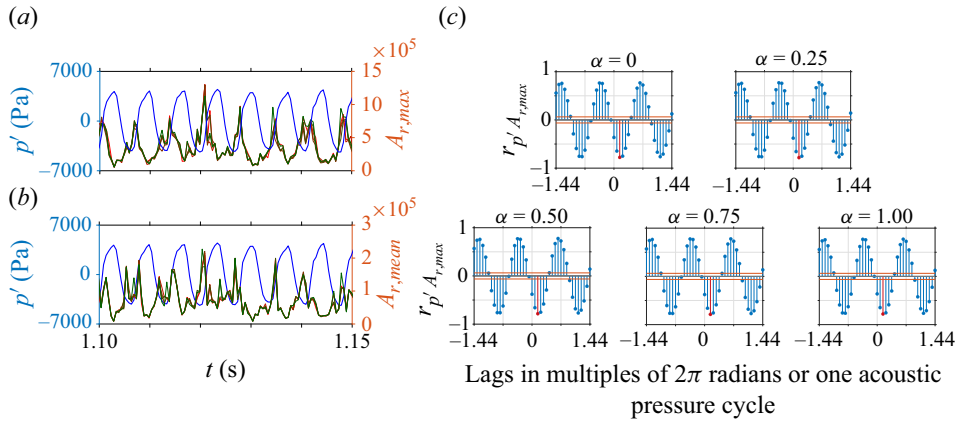


Figure 14. Time series showing the variation of the (*a*) mean ($A_{r,mean}$) and (*b*) maximum ($A_{r,max}$) of all inter-community interactions during the state of thermoacoustic instability. The acoustic pressure fluctuations are shown in blue. (*c*) Shows the cross-correlation between p' and $A_{r,max}$, denoted by $r_{p'A_{r,max}}$ and the corresponding lags in terms of multiples of acoustic pressure cycles (2π rad is equivalent to one acoustic pressure cycle) and degrees. The minima of $r_{p'A_{r,max}}$ is at 52°, indicating the lag between the occurrences of p' minima (i.e., vortex shedding from the backward-facing step) and maximum of vortical interactions. We observe that the phase lag of 52° is independent of the value of α used to construct vortical networks.

The vorticity field for the four data points marked is shown in (*c*), and each column of (*d*) illustrates the maximum-interacting pair of communities for different α values. The two different colour schemes denote the in- and out-strength distribution of the inter-community edge weights.

The pair of communities with the largest inter-community interaction remains consistent as α changes from 0 to 1. However, the direction of links between the two communities reverses as α changes. This occurs since $u_{i\to j} = A_{ji}$ for $\alpha = 0$, and $u_{i\to j} = A_{ij}$ for $\alpha = 1$. This reversal is evident from the opposite colour schemes of the two interacting communities for $\alpha = 0$ and $\alpha = 1$.

D.2. *Phase lag between p' oscillations and network measures*

The phase lag shows minor sensitivity to variations in α since the statistics of inter-community interactions, such as their mean ($A_{r,mean}$) and maximum ($A_{r,max}$) values, change only in magnitude. The temporal patterns of inter-community interactions, that is, the time instants at which these interactions reach their local minima or maxima, remain consistent as the effect of changing α on the network weights occurs uniformly through the vortical network at each time instant.

Figure 14(*a*,*b*) show the variation of acoustic pressure oscillations and the mean and the maximum of all inter-community interactions for 100 time instants. The phase lag remains almost constant for all α values. This is further corroborated in figure 14(*c*) where we plot the cross-correlations between p' and $A_{r,max}$ for different values of α. The minima of p' fluctuations correspond to the instants of vortex shedding. The minima of cross-correlation closest to 0° in figure 14(*c*) indicates the phase lag where p' and $A_{r,max}$ are maximum negatively correlated. We consider maximum negative correlation since the minima of p' fluctuations and maxima of $A_{r,max}$ are used for computing the cross-correlation. We observe a consistent phase lag of about 52° between the instants of vortex shedding and the maximum inter-community interactions for all the values of α considered.

https://doi.org/10.1017/jfm.2025.10362 Published online by Cambridge University Press

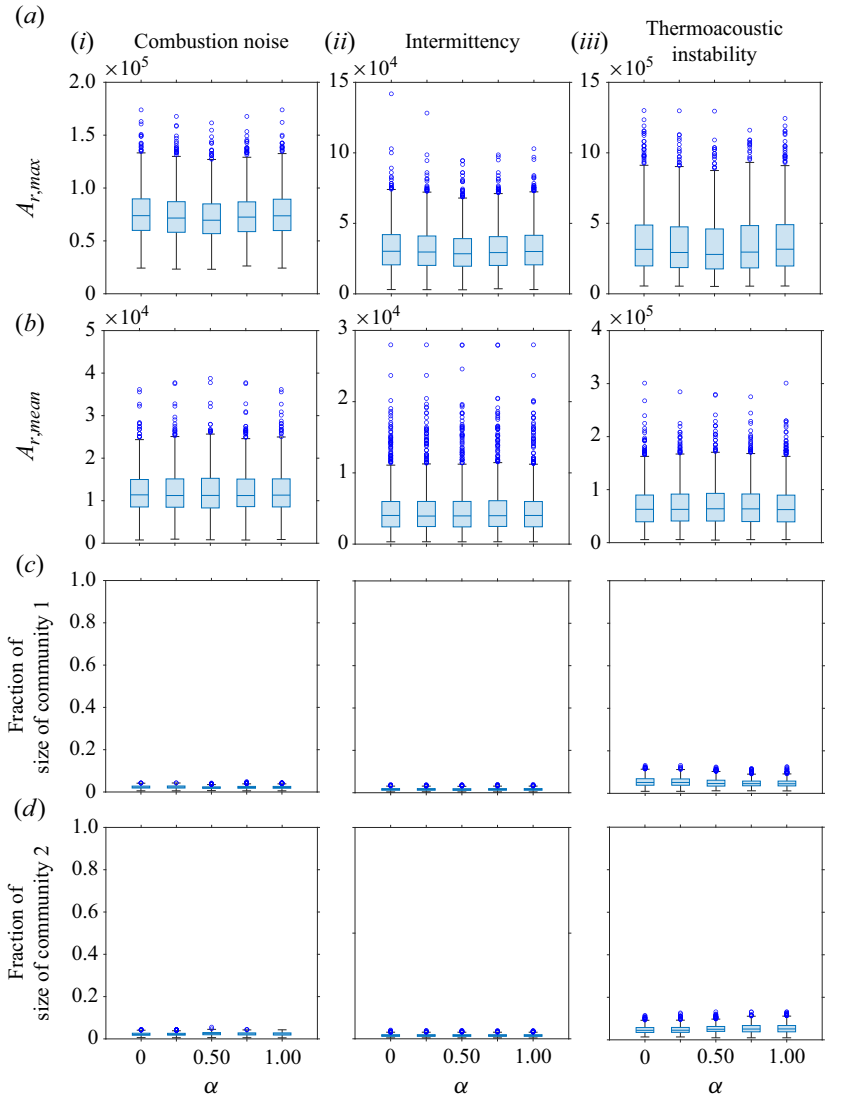


Figure 15. Panels (*a*) and (*b*) show the box plots of $A_{r,max}$ and $A_{r,mean}$ for 1000 data points calculated for five α values during the states of (*i*) combustion noise, (*ii*) intermittency and (*iii*) thermoacoustic instability. We observe minute changes in the distribution of the inter-community interaction measures as α is varied. Panels (*c*) and (*d*) show the variation of the fraction of the size of the two communities with maximum inter-community interaction with a change in the value of α. The consistent low value of this fraction indicates the low sensitivity of the sizes of communities with maximum inter-community interaction towards different α values between 0 and 1.

D.3. *Statistics of inter-community interactions and sizes of communities with the largest interaction*

Finally, we look at the effect of α on the distribution of the mean and maximum of inter-community interactions and on the size of the two communities with the maximum inter-community interaction.

Figure 15(*a*,*b*) shows the variation of the distribution of the inter-community interaction measures calculated for 1000 data points present during all the three dynamical states with

https://doi.org/10.1017/jfm.2025.10362 Published online by Cambridge University Press

a change in the values of α considered while constructing vortical networks. We observe negligible changes in the distributions of $A_{r,max}$ and $A_{r,mean}$, indicating that the network measures do not vary significantly as α is varied from 0 to 1. Similarly, the size of the communities with maximum inter-community interaction (named 'community 1' and 'community 2' in figure 15*c*,*d*) does not change significantly with a change in the values of α, as seen in figure 15(*c*,*d*).

Thus, we infer that the variation of α does not significantly vary the results shown in the present study. However, we emphasise using $\alpha = 0$ to maintain the unidirectional (directed) influencing capability of the vortical structures.

References

Altay, H.M., Hudgins, D.E., Speth, R.L., Annaswamy, A.M. & Ghoniem, A.F. 2010 Mitigation of thermoacoustic instability utilizing steady air injection near the flame anchoring zone. *Combust. Flame* **157** (4), 686–700.

Altay, M., Speth, R., Snarheim, D., Hudgins, D., Ghoniem, A.F. & Annaswamy, A.M. 2007 Impact on microjet actuation on stability of a backward-facing step combustor. In *45th AIAA Aerospace Sciences Meeting and Exhibit*, pp. AIAA–2007-0563. American Institute of Aeronautics and Astronautics.

Barabási, A. 2012 The network takeover. *Nat. Phys.* **8** (1), 14–16.

Blondel, V.D., Guillaume, J.-L., Lambiotte, R. & Lefebvre, E. 2008 Fast unfolding of communities in large networks. *J. Stat. Mech.: Theory Exp.* **2008** (10), P10008.

Candel, S., Durox, D. & Schuller, T. 2004 Flame interactions as a source of noise and combustion instabilities. AIAA.

Castagliola, P., Achouri, A., Taleb, H., Celano, G. & Psarakis, S. 2013 Monitoring the coefficient of variation using a variable sampling interval control chart. *Qual. Reliab. Engng Intl* **29** (8), 1135–1149.

Coats, C.M. 1996 Coherent structures in combustion. *Prog. Energy Combust. Sci.* **22** (5), 427–509.

Cordeiro, M., Sarmento, R.P. & Gama, J. 2016 Dynamic community detection in evolving networks using locality modularity optimization. *Soc. Netw. Anal. Min.* **6** (1), 1–20.

Desai, R., Chakravarthy, S. & Ramgopal, S. 2010 Effect of fuel injection location on combustion instability in a dump combustor. In *48th AIAA Aerospace Sciences Meeting Including the New Horizons Forum and Aerospace Exposition*, pp. 216. American Institute of Aeronautics and Astronautics.

Fiedler, H.E. 1988 Coherent structures in turbulent flows. *Prog. Aerosp. Sci.* **25** (3), 231–269.

Fortunato, S. 2010 Community detection in graphs. *Phys. Rep.* **486** (3–5), 75–174.

Fortunato, S. & Barthelemy, M. 2007 Resolution limit in community detection. *Proc. Natl Acad. Sci.* **104** (1), 36–41.

Fruchterman, T.M.J. & Reingold, E.M. 1991 Graph drawing by force-directed placement. *Softw. Pract. Exp.* **21** (11), 1129–1164.

Geikie, M.K. & Ahmed, K.A. 2018 Pressure-gradient tailoring effects on the turbulent flame-vortex dynamics of bluff-body premixed flames. *Combust. Flame* **197**, 227–242.

Geikie, M.K., Rising, C.J., Morales, A.J. & Ahmed, K.A. 2021 Turbulent flame-vortex dynamics of bluff-body premixed flames. *Combust. Flame* **223**, 28–41.

George, N.B., Unni, V.R., Raghunathan, M. & Sujith, R.I. 2018 Pattern formation during transition from combustion noise to thermoacoustic instability via intermittency. *J. Fluid Mech.* **849**, 615–644.

Ghoniem, A.F., Annaswamy, A.M., Park, S. & Sobhani, Z.C. 2005 Stability and emissions control using air injection and H2 addition in premixed combustion. *Proc. Combust. Inst.* **30** (2), 1765–1773.

Gopalakrishnan Meena, M., Nair, A.G. & Taira, K. 2018 Network community-based model reduction for vortical flows. *Phys. Rev. E* **97** (6), 063103.

Gopalakrishnan Meena, M. & Taira, K. 2021 Identifying vortical network connectors for turbulent flow modification. *J. Fluid Mech.* **915**, A10.

Guimerà, R. & Amaral, L.A.N. 2005 Functional cartography of complex metabolic networks. *Nature* **433** (7028), 895–900.

Gürcan, Ö.D. 2017 Nested polyhedra model of turbulence. *Phys. Rev. E* **95** (6), 063102.

Gürcan, Ö.D. 2018 Nested polyhedra model of isotropic magnetohydrodynamic turbulence. *Phys. Rev. E* **97** (6), 063111.

Hadjighasem, A., Karrasch, D., Teramoto, H. & Haller, G. 2016 Spectral-clustering approach to Lagrangian vortex detection. *Phys. Rev. E* **93** (6), 063107.

Ho, C.M. & Huerre, P. 1984 Perturbed free shear layers. *Annu. Rev. Fluid Mech.* **16** (1), 365–424.

https://doi.org/10.1017/jfm.2025.10362 Published online by Cambridge University Press

HONG, S., SPETH, R.L., SHANBHOGUE, S.J. & GHONIEM, A.F. 2013 Examining flow-flame interaction and the characteristic stretch rate in vortex-driven combustion dynamics using PIV and numerical simulation. *Combust. Flame* **160** (8), 1381–1397.

HUSSAIN, A.K.M.F. 1983 Coherent structures–reality and myth. *Phys. Fluids* **26** (10), 2816–2850.

HUSSAIN, A.K.M.F. 1986 Coherent structures and turbulence. *J. Fluid Mech.* **173**, 303–356.

HUSSAIN, M., JAMSHED, S. & OZAIR, M. 2022 Simulations and analysis of vortex driven combustion instability. In *2022 19th International Bhurban Conference on Applied Sciences and Technology (IBCAST)*, pp. 765–770. IEEE.

IACOBELLO, G., RIDOLFI, L. & SCARSOGLIO, S. 2021 A review on turbulent and vortical flow analyses via complex networks. *Phys. A: Stat. Mech. Appl.* **563**, 125476.

IACOBELLO, G., SCARSOGLIO, S., KUERTEN, J.G.M. & RIDOLFI, L. 2019 Lagrangian network analysis of turbulent mixing. *J. Fluid Mech.* **865**, 546–562.

IACOBELLO, G., SCARSOGLIO, S. & RIDOLFI, L. 2018 Visibility graph analysis of wall turbulence time-series. *Phys. Lett. A* **382** (1), 1–11.

JADHAV, V., GUTTAL, V. & MASILA, D.R. 2022 Randomness in the choice of neighbours promotes cohesion in mobile animal groups. *R. Soc. Open Sci.* **9** (3), 220124.

KARRER, B., LEVINA, E. & NEWMAN, M.E. 2008 Robustness of community structure in networks. *Phys. Rev. E* **77** (4), 046119.

KAWANO, K., GOTODA, H., NABAE, Y., OHMICHI, Y. & MATSUYAMA, S. 2023 Complex-network analysis of high-frequency combustion instability in a model single-element rocket engine combustor. *J. Fluid Mech.* **959**, A1.

KRISHNAN, A., MANIKANDAN, R., MIDHUN, P.R., REEJA, K.V., UNNI, V.R., SUJITH, R.I., MARWAN, N. & KURTHS, J. 2019*a* Mitigation of oscillatory instability in turbulent reactive flows: A novel approach using complex networks. *EPL (Europhys. Lett.)* **128** (1), 14003.

KRISHNAN, A., SUJITH, R., MARWAN, N. & KURTHS, J. 2021 Suppression of thermoacoustic instability by targeting the hubs of the turbulent networks in a bluff body stabilized combustor. *J. Fluid Mech.* **916**, A20.

KRISHNAN, A., SUJITH, R.I., MARWAN, N.K. & J 2019*b* On the emergence of large clusters of acoustic power sources at the onset of thermoacoustic instability in a turbulent combustor. *J. Fluid Mech.* **874**, 455–482.

LANCICHINETTI, A. & FORTUNATO, S. 2011 Limits of modularity maximization in community detection. *Phys. Rev. E* **84** (6), 066122.

LANCICHINETTI, A., FORTUNATO, S. & RADICCHI, F. 2008 Benchmark graphs for testing community detection algorithms. *Phys. Rev. E* **78** (4), 046110.

LEICHT, E.A. & NEWMAN, M.E.J. 2008 Community structure in directed networks. *Phys. Rev. Lett.* **100** (11), 118703.

MALMENDIER, A. & REID, J.T. 2020 Application of the Biot–Savart law to parabolic vortex segments using elliptic integrals. *Zeitschrift für Angewandte Mathematik Und Physik* **71** (4), 1–20.

MANKBADI, R. & LIU, J.T.C. 1984 Sound generated aerodynamically revisited: large-scale structures in a turbulent jet as a source of sound. *Philos. Trans. R. Soc. A* **311** (1516), 183–217.

MEILĂ, M. 2007 Comparing clusterings–an information based distance. *J. Multivar. Anal.* **98** (5), 873–895.

MONDAL, S., UNNI, V.R. & SUJITH, R.I. 2017 Onset of thermoacoustic instability in turbulent combustors: an emergence of synchronized periodicity through formation of chimera-like states. *J. Fluid Mech.* **811**, 659–681.

MURAYAMA, S., KINUGAWA, H., TOKUDA, I.T. & GOTODA, H. 2018 Characterization and detection of thermoacoustic combustion oscillations based on statistical complexity and complex-network theory. *Phys. Rev. E* **97** (2), 022223.

NAIR, A.G., BRUNTON, S.L. & TAIRA, K. 2018 Networked-oscillator-based modeling and control of unsteady wake flows. *Phys. Rev. E* **97** (6), 063107.

NAIR, A.G. & TAIRA, K. 2015 Network-theoretic approach to sparsified discrete vortex dynamics. *J. Fluid Mech.* **768**, 549–571.

NAIR, S. & LIEUWEN, T. 2007 Near-blowoff dynamics of a bluff-body stabilized flame. *J. Propul. Power* **23** (2), 421–427.

NAIR, V., THAMPI, G. & SUJITH, R.I. 2014 Intermittency route to thermoacoustic instability in turbulent combustors. *J. Fluid Mech.* **756**, 470–487.

NEAMTU-HALIC, M.M., KRUG, D., HALLER, G. & HOLZNER, M. 2019 Lagrangian coherent structures and entrainment near the turbulent/non-turbulent interface of a gravity current. *J. Fluid Mech.* **877**, 824–843.

NEWMAN, M. 2018 *Networks*. Oxford University Press.

NEWMAN, M.E.J. 2004 Fast algorithm for detecting community structure in networks. *Phys. Rev. E* **69** (6), 066133.

https://doi.org/10.1017/jfm.2025.10362 Published online by Cambridge University Press

NEWMAN, M.E.J. & GIRVAN, M. 2004 Finding and evaluating community structure in networks. *Phys. Rev. E* **69** (2), 026113.

POINSOT, T.J., TROUVE, A.C., VEYNANTE, D.P., CANDEL, S.M. & ESPOSITO, E.J. 1987 Vortex-driven acoustically coupled combustion instabilities. *J. Fluid Mech.* **177**, 265–292.

PREMCHAND, C., KRISHNAN, A., RAGHUNATHAN, M., MIDHUN, P., REEJA, K., SUJITH, R. & NAIR, V. 2024 Identifying optimal location for control of thermoacoustic instability through statistical analysis of saddle point trajectories. *Chaos: Interdisciplinary J. Nonlinear Sci.* **34** (8), 083113.

RAFFEL, M. *et al.* 1998 *Particle Image Velocimetry: A Practical Guide*. Springer.

REICHARDT, J. & BORNHOLDT, S. 2006 Statistical mechanics of community detection. *Phys. Rev. E* **74** (1), 016110.

RENARD, P.H., THEVENIN, D., ROLON, J.C. & CANDEL, S. 2000 Dynamics of flame/vortex interactions. *Prog. Energy Combust. Sci.* **26** (3), 225–282.

RISING, C.J., MORALES, A.J., GEIKIE, M.K. & AHMED, K.A. 2021 The effects of turbulence and pressure gradients on vorticity transport in premixed bluff-body flames. *Phys. Fluids* **33** (1), 017106.

ROGERS, D.E. & MARBLE, F.E. 1956 A mechanism for high-frequency oscillation in ramjet combustors and afterburners. *J. Jet Propuls.* **26** (6), 456–462.

ROY, A., PREMCHAND, C.P., RAGHUNATHAN, M., KRISHNAN, A., NAIR, V. & SUJITH, R.I. 2021 Critical region in the spatiotemporal dynamics of a turbulent thermoacoustic system and smart passive control. *Combust. Flame* **226**, 274–284.

SCHADOW, K.C. & GUTMARK, E. 1992 Combustion instability related to vortex shedding in dump combustors and their passive control. *Prog. Energy Combust. Sci.* **18** (2), 117–132.

SER-GIACOMI, E., ROSSI, V., LÓPEZ, C. & HERNÁNDEZ-GARCIA, E. 2015 Flow networks: a characterization of geophysical fluid transport. *Chaos* **25** (3), 036404.

SHANBHOGUE, S.J., SEELHORST, M. & LIEUWEN, T. 2009 Vortex phase-jitter in acoustically excited bluff body flames. *Intl J. Spray Combust. Dyn.* **1** (3), 365–387.

SIVAKUMAR, R. & CHAKRAVARTHY, S. 2008 Experimental investigation of the acoustic field in a bluff-body combustor. *Intl J. Aeroacoust.* **7** (3–4), 267–299.

SMITH, D.A. & ZUKOSKI, E.E. 1985 Combustion instability sustained by unsteady vortex combustion. In *21st Joint Propulsion Conference*, AIAA.

SMITH, K., BRIGHTON, H. & KIRBY, S. 2003 Complex systems in language evolution: the cultural emergence of compositional structure. *Adv. Complex Syst.* **6** (04), 537–558.

SUJITH, R.I. & PAWAR, S.A. 2021 *Thermoacoustic Instability*. Springer Series in Synergetics.

TACHIBANA, S., ZIMMER, L., KUROSAWA, Y. & SUZUKI, K. 2007 Active control of combustion oscillations in a lean premixed combustor by secondary fuel injection coupling with chemiluminescence imaging technique. *Proc. Combust. Inst.* **31** (2), 3225–3233.

TAIRA, K. & NAIR, A.G. 2022 Network-based analysis of fluid flows: progress and outlook. *Prog. Aerosp. Sci.* **131**, 100823.

TAIRA, K., NAIR, A.G. & BRUNTON, S.L. 2016 Network structure of two-dimensional decaying isotropic turbulence. *J. Fluid Mech.* **795**, R2.

TANDON, S. & SUJITH, R.I. 2023 Multilayer network analysis to study complex inter-subsystem interactions in a turbulent thermoacoustic system. *J. Fluid Mech.* **966**, A9.

TIETJENS, O.K.G. & PRANDTL, L. 1957 Applied hydro-and aeromechanics: based on lectures of L. Prandtl, vol. **2**, Courier Corporation.

UHM, J.H. & ACHARYA, S. 2005 Low-bandwidth open-loop control of combustion instability. *Combust. Flame* **142** (4), 348–363.

YEH, C.A., GOPALAKRISHNAN MEENA, M. & TAIRA, K. 2021 Network broadcast analysis and control of turbulent flows. *J. Fluid Mech.* **910**, A15.

YU, K.H. & SCHADOW, K.C. 1997 Role of large coherent structures in turbulent compressible mixing. *Exp. Therm. Fluid Sci.* **14** (1), 75–84.

YU, K.H., TROUVÉ, A. & DAILY, J.W. 1991 Low-frequency pressure oscillations in a model ramjet combustor. *J. Fluid Mech.* **232**, 47–72.

ZILITINKEVICH, S. 1970 Non-local turbulent transport: pollution dispersion aspects of coherent structure of connective flows. *WIT Trans. Ecol. Environ.* **9**, 53–60.

ZOU, Y., DONNER, R.V., MARWAN, N., DONGES, J.F. & KURTHS, J. 2019 Complex network approaches to nonlinear time series analysis. *Phys. Rep.* **787**, 1–97.

https://doi.org/10.1017/jfm.2025.10362 Published online by Cambridge University Press